Graphical Abstract

Synthesis

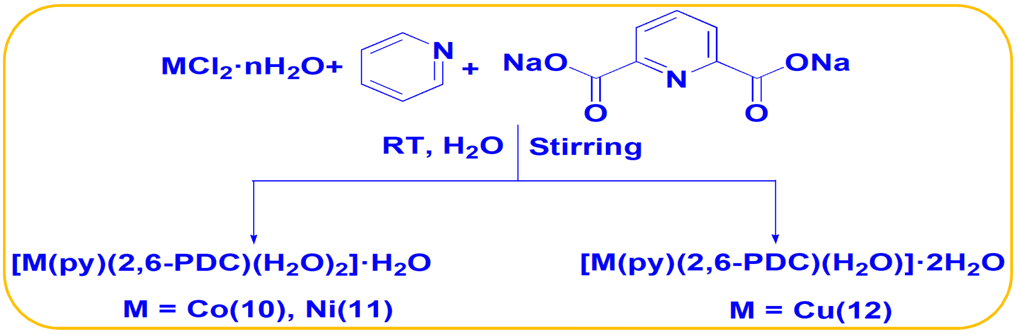

$[M(py)(2,6\text{-}PDC)(H_2O)_2]\cdot H_2O$

M = Co(10), Ni(11)

$[M(py)(2,6\text{-}PDC)(H_2O)]\cdot 2H_2O$

M = Cu(12)

Molecular Structures

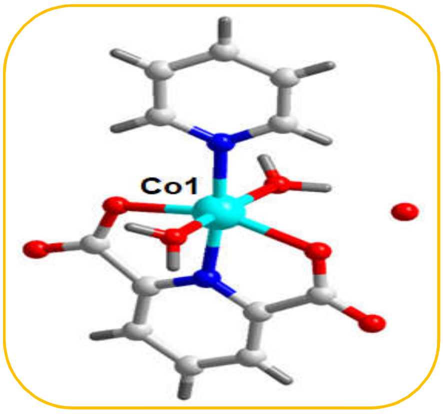

10

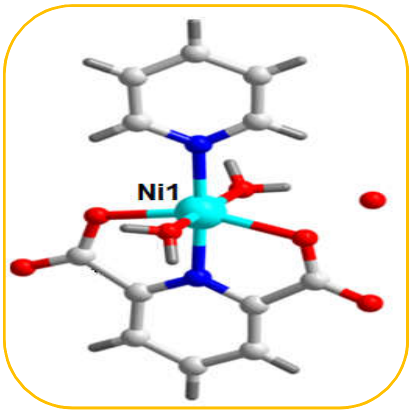

11

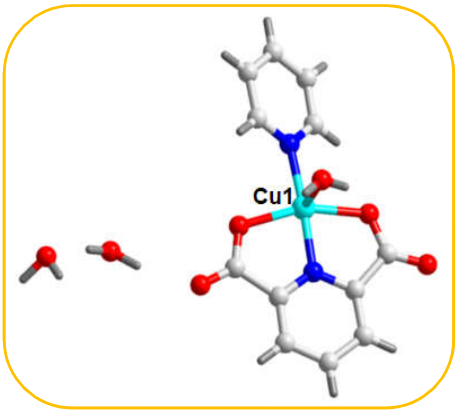

12

Self-Assembly

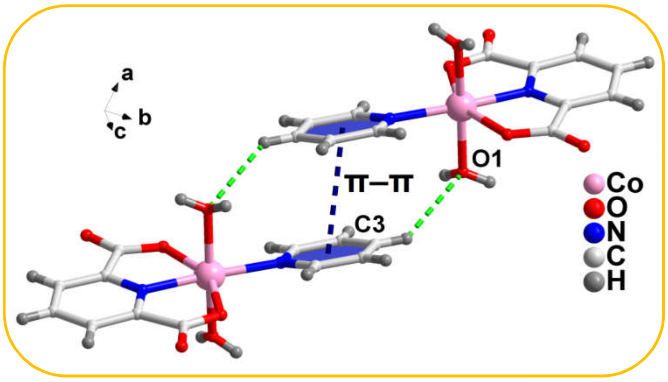

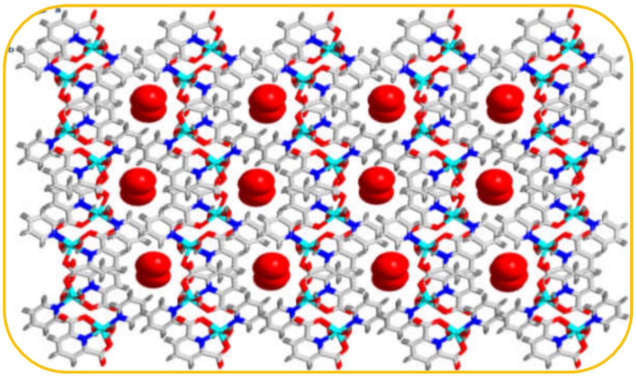

Apoptosis and MTT Assays

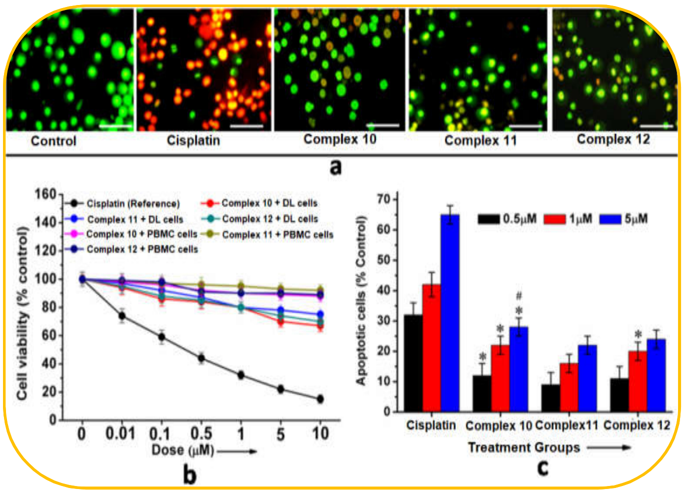

NCI plot

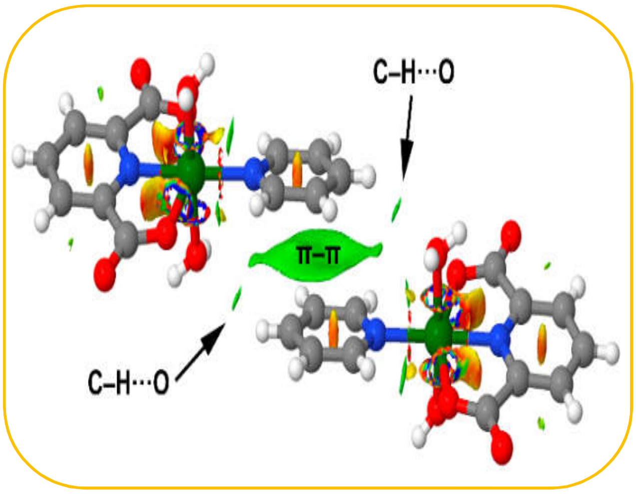

Chapter 5

Synthesis, Structural investigations and Supramolecular Assemblies in Coordination Compounds of Co(II), Ni(II) and Cu(II) involving 2,6-Pyridinedicarboxylate: Antiproliferative Evaluation and Theoretical Studies

5.1 INTRODUCTION

Supramolecular architectures involving metal-organic moieties have received much emphasis in the field of crystal engineering because of their potential applications as optical, electrical, magnetic, catalytic and adsorptive materials.[1,2] In recent years, researchers are trying to develop non-covalent supramolecular interactions as a powerful tool for the formation of interesting and fascinating structures of coordination compounds.[3-5] The literature shows that the self assembly processes via non-covalent interactions offer the possibility to construct interesting network architectures by assembling organic moieties involving transition metals.[6] Despite the upsurge in the construction of diverse architectures, the control of dimensionality is still a major challenge in this field[7] due to the fact that the network topologies of such molecular building blocks are usually controlled and modified by the selection of the coordination geometry of the central metal[8], the structural diversity of organic moieties as ligands[9], the nature of solvent used[10] and the ratio of metal salt to organic ligands.[11]

It is possible to design and construct desired structures of coordination complexes by the proper choice of the organic moieties and the central metals.[12] Since long, neutral and rigid N-donor molecules such as pyridine have been widely used to construct supramolecular architectures along with various anionic species that compensate the charge of the resulting metal-organic frameworks.[13] Many examples of neutral aromatic N-donor ligands are explored that facilitate the construction of diverse coordination compounds with interesting one-, two- and three-dimensional network architectures.[14] The transition metal complexes involving pyridine dicarboxylates provide the possibility of formation of diverse supramolecular assemblies with structural varieties because of the multiple coordination modes as anions.[15-17] Tella *et al*. have reported a luminescent octahedral zinc(II) complex of pyridine-2,6-dicarboxylate *viz*. $[Zn(II)(Tpy)(2,6\text{-}PDC)]\cdot 4H_2O$ [where, Tpy = 2,2′,6′,2″-terpyridine and 2,6-PDC = pyridine-2.6-dicarboxylate].[18] Moschovitis *et al*. have reported the catalytic activity on catechol oxidation of three coordination complexes of copper involving pyridine-2,6-dicarboxylate *viz*. $[Cu(I)(2,6\text{-}PDC)(TPP)_2]\cdot H_2O$, $[Cu(II)(2,6\text{-}PDC)(H_2\text{-}2,6\text{-}PDC)]$ and $\{[Cu(II)(2,6\text{-}PDC)(H_2\text{-}2,6\text{-}PDC)][Cu(I)(TPP)_3]_2\}\cdot 2DMSO$ [where, TPP = triphenylphosphine, DMSO = dimethyl sulfoxide, 2,6-PDC = pyridine-2.6-dicarboxylate].[19] Garin and her research group have also reported two novel coordination solids of Co(III) and Cr(III) involving monosubstituted pyridine-2,6-dicarboxylic acid hydrazide derivative, *viz*. CoL and CrL [where, H_2L = 6-{[2-(phenylcarbonyl)hydrazino]-carbonyl}pyridine-2-carboxylic acid].[20]

The discovery of metal-organic compounds involving carboxylates attracted researchers because of their wide applications in various fields of biology, *viz*. antiproliferative, anti-bacterial, anti-fungal and in catalysis.[21-22] Metal-organic compounds of aromatic carboxylate ligands are believed to exhibit biological activity due to intercalation of DNA of the target biomolecules via hydrogen bonding and π stacking interactions.[23] Two new coordination polymers of aminopyridine-2-carboxylate ligand, *viz*. $\{[CoK(ampy)_3(H_2O)_3]\cdot 3H_2O\}_n$ and $[Cu(ampy)_2]_n$ [where, ampy = aminopyridine-2-carboxylate] have been recently reported to exhibit *in vitro* antiproliferative activities.[24] Bordbar and his group have reported the concentration-dependent cancer cell growth inhibition by a new Co(II) pyridine-based complex *viz*. $[Co(amp)(2,6\text{-}PDC)(H_2O)_2]\cdot H_2O$ [where, amp = 2-aminopyridine].[25] Wang *et al*. have highlighted the role of Sn(II) and also the carboxylate group of 2,6-pyridinedicarboxylate in the antiproliferative activity of a Sn(II) coordination solid *viz*. bis(triorganotin)-2,6-pyridinedicarboxylate against Hela (cervix tumor cell) and MCF-7 (mammary tumor cell) cancer cell lines.[26] Catalytic performance of the coordination polymers involving 2,6-pyridinedicarboxylate *viz*. $[Cu(2,6\text{-}PDC)(H_2O)_{1.5}]_n$ and $[Mn(2,6\text{-}PDC)(H_2O)_{1.5}]_n$ towards degradation of methylene blue and methyl orange in the presence of hydrogen peroxide has also been reported recently.[27]

Supramolecular association of aromatic systems has attracted considerable attention due to the utilization of intermolecular non-covalent contacts that relied upon for the design and development of bioactive materials.[28] In biology, these interactions are the basis of a great deal of processes, whose efficiency is always impressive. The role of aromatic interactions becomes prominent in drug-receptor interactions, crystal engineering and protein folding.[29] Aromatic π-stacking between aromatic rings is imperative in the construction of flexible materials based on aromatic compounds.[30] The importance of π-stacking assemblies in metal complexes between systems containing aromatic rings that range from large biological systems to relatively small molecules has recently been reported.[31,32] There are examples of supramolecular architectures involving N-donor aromatic ligands that exhibit excellent bio-activity via multiple supramolecular interactions with DNA by the use of π-π stacking, hydrophobic effect and hydrogen bonding interactions.[33] Qin *et al*. have reported the effect of anti-parallel π-stacking interactions in inducing cytotoxicity against cancer cells for the coordination compound [$Cu(C_{12}H_8N_2)(C_{12}H_{11}O_4N)]\cdot 4H_2O$ [where, $C_{12}H_8N_2$ = 1,10′-phenanthroline and $C_{12}H_{11}O_4N$ = b-[(3-formyl-5-methyl-2-hydroxy-benzylidene)-amino]propionic acid].[34] Yeasin and her research group have also reported the *in vitro* antiproliferative activity of a doubly chloro bridged dimeric copper(II) complex *viz.* [$Cu_2(\mu\text{-}Cl)_2(HL)_2Cl_2$] [where, HL = 5-[(pyridin-2-ylmethylene)-amino]-pentan-1-ol)], which is stabilized by anti-parallel π-stacking interactions.[35]

In the present chapter, we have described the synthesis, crystal structures and antiproliferative evaluation of three monomeric divalent metal complexes involving 2,6-pyridinedicarboxylate and pyridine, *viz.* [$Co(py)(2,6\text{-}PDC)(H_2O)_2]\cdot H_2O$ (**10**); [$Ni(py)(2,6\text{-}PDC)(H_2O)_2]\cdot H_2O$ (**11**) and [$Cu(py)(2,6\text{-}PDC)(H_2O)]\cdot 2H_2O$ (**12**) [where, py = pyridine, PDC = pyridinedicarboxylate]. Apart from discussing the synthesis and crystal structures of the compounds, we also aim to explore the various non-covalent supramolecular interactions that may govern the stability of the structures. In all the three complexes, the coordinated *py* establishes anti-parallel π-stacking interactions generating self-assembled complex dimers in the solid state. We also aim to highlight the isostructurality parameters of the compounds **10** and **11** using Fabian & Kalman approach. We have used DFT calculations to investigate the influence of the transition metals on the binding energies of the anti-parallel π-stacking interactions. We have investigated the antiproliferative potential of the compounds in Dalton’s Lymphoma (DL) cell line by MTT and apoptosis assays. *In silico*-docking simulation and the pharmacophore features based on structure activity relationship (SAR) have been performed with apoptosis regulator proteins for the identification of possible molecular mode of action of the synthesized complexes.

5.2 EXPERIMENTAL

5.2.1 Materials and methods

All the metal chloride salts and the ligands used to synthesize compounds **10**, **11** and **12** were obtained from Sigma Aldrich and Merck (India) Ltd. All the reactions were carried out in de-ionized water medium. Elemental (C, H and N) analyses were carried out by using a Perkin Elmer 2400 Series II CHNS/O analyzer. FT-IR spectra were recorded in a Brukar APEX II FT-IR spectrophotometer within the range from 4000 to 500 cm^{-1}. The electronic spectra were recorded by using a Shimadzu UV-2600 spectrophotometer. $BaSO_4$ powder was used as reference (100% reflectance) for UV-Vis-NIR spectral analyses. Thermogravimetric studies were carried out under the flow of N_2 gas using Mettler Toledo TGA/DSC1 STAR^e system at the heating rate of 10°C min^{-1}. The powder X-ray diffraction (PXRD) data were recorded in XPERT-PRO X-ray powder diffractometer with Cu-Kα radiation. Room temperature magnetic susceptibility was measured at 300 K on a Sherwood Mark 1 Magnetic Susceptibility balance by Evans method.

5.2.2 Preparation of the complexes

5.2.2.1 Preparation of $[Co(py)(2,6\text{-}PDC)(H_2O)_2]\cdot H_2O$ (10)

The compound **10** was prepared by stiring an aqueous solution of cobalt(II) chloride hexahydrate, $CoCl_2\cdot 6H_2O$ (1.0 mmol, 0.238 g), pyridine (1.0 mmol, 0.08 mL) and disodium salt of 2,6-pyridinedicarboxylic acid (1.0 mmol, 0.211 g) (**Scheme 5.1**) at room temperature for two hours. The red coloured compound so obtained was then filtered and the filtrate left unperturbed for crystallization. After about one week, block shaped, reddish single crystals of compound **10** suitable for X-ray analysis were obtained. The large crystals were filtered off, washed with small portion of water and dried at ambient temperature in air. Yield: 0.31 g (87%). Anal. calcd. for $C_{12}H_{12}CoN_2O_7$

(Mw = 355.17): C, 40.58%; H, 3.41%; N, 7.89%. Found: C, 40.51%; H, 3.30%; N, 7.82%. IR spectral data (KBr disc, cm^{-1}): 3266(br), 2301(m), 2010(w), 1933(w), 1868(w), 1613(s), 1432(sh), 1363(s), 1279(s), 1183(s), 1070(s), 1038(s), 915(s), 820(sh), 760(s), 735(s), 691(s), 529(m) [s, strong; m, medium; w, weak; br, broad; sh, shoulder]. μ_{eff} = 3.87 BM.

5.2.2.2 Preparation of [Ni(py)(2,6-PDC)(H_2O)$_2$]·H_2O (11)

The synthesis of **11** is similar to that of **10** except for cobalt(II) chloride hexahydrate now substituted by nickel(II) chloride hexahydrate, $NiCl_2 \cdot 6H_2O$ (1.0 mmol, 0.237 g) (**Scheme 5.1**). The green coloured compound obtained was filtered and the filtrate was left unperturbed in cooling condition for crystallization. After about two weeks, block shaped, blue single crystals of compound **11** suitable for X-ray analysis were obtained. The large crystals were filtered off, washed with small portion of water and dried at ambient temperature in air. Yield: 0.29 g (82%). Anal. calcd. for $C_{12}H_{12}N_2NiO_7$ (Mw = 354.94): C, 40.61%; H, 3.41%; N, 7.89%. Found: C, 40.53%; H, 3.28%; N, 7.76%. IR spectral data (KBr disc, cm^{-1}): 3257(br), 2282(m), 2012(w), 1931(w), 1869(w), 1631(s), 1488(sh), 1434(s), 1386(s), 1360(s), 1276(s), 1216(w), 1185(w), 1155(w), 1080(s), 1041(sh), 921(w), 822(sh), 769(s), 739(s), 694(s), 635(sh), 542(sh) [s, strong; m, medium; w, weak; br, broad; sh, shoulder]. μ_{eff} = 2.81 BM.

5.2.2.3 Preparation of [Cu(py)(2,6-PDC)(H_2O)]·$2H_2O$ (12)

Compound **12** was synthesized in a way similar to that of **10** except for cobalt(II) chloride hexahydrate replaced by copper(II) chloride dihydrate, $CuCl_2 \cdot 2H_2O$ 1.0 mmol, 0.170 g) (**Scheme 5.1**). The blue coloured compound so obtained was then filtered and the filtrate left unperturbed for crystallization. After about one week, block shaped, blue single crystals of compound **12** suitable for X-ray analysis were obtained. The large crystals were filtered off, washed with small portion of water and dried at ambient temperature in air. Yield: 0.32 g (89%). Anal. calcd. for $C_{12}H_{14}CuN_2O_7$ (Mw = 361.79): C, 39.84%; H, 3.90%; N, 7.74%. Found: C, 39.72%; H, 3.83%; N, 7.71%. IR spectral data (KBr disc, cm^{-1}): 3430(br), 3098(s), 2017(w), 1949(w), 1889(w), 1678(s), 1631(s), 1488(s), 1451(s), 1420(sh), 1345(s), 262(sh), 1216(s), 1179(s), 1148(s), 1080(s), 1049(sh), 1019(m), 958(w), 905(s), 853(m), 816(s), 785(s), 733(s), 703(s), 680(s), 589(w), 550(w) [s, strong; m, medium; w, weak; br, broad; sh, shoulder]. μ_{eff} = 1.74 BM.

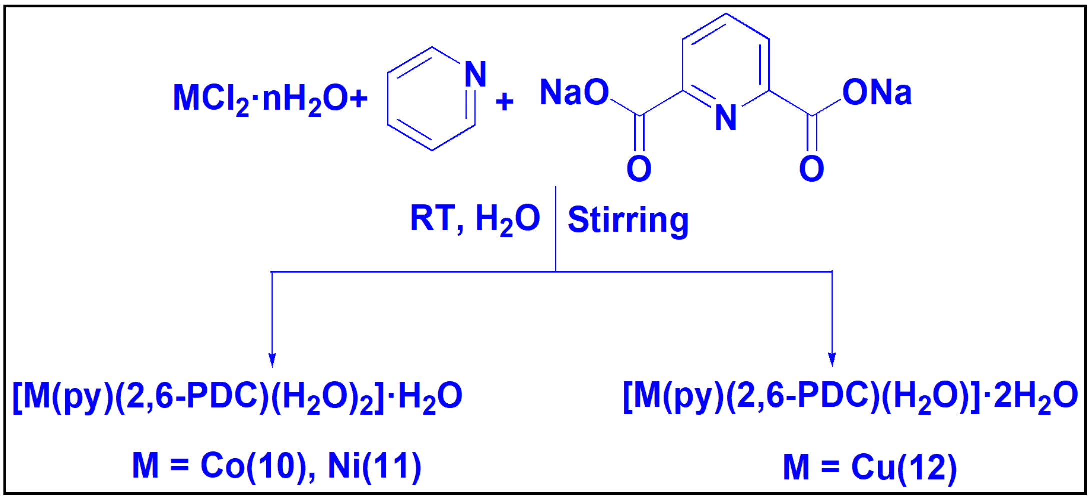

Scheme 5.1 Synthesis of the complexes **10**, **11** and **12**.

5.2.3 X-ray crystallographic procedures

Molecular and crystal structures of the complexes **10**, **11** and **12** were determined by single crystal X-ray diffraction technique. Collection of X-ray crystallographic data and analyses of crystal structures have been done as detailed in Chapter 2. X-ray diffraction data collection was carried out on a Bruker SMART CCD diffractometer with graphite monochromatised Mo Kα radiation (λ = 0.71073 Å). Semiempirical absorption correction, as well as scaling and merging the different datasets for each wavelength were performed with SADABS.[36] Crystal structures were solved by direct method (SHELXS) and refined by full matrix least squares techniques (SHELXL-2018/3) using the WinGX[37] platform available for personal computers. All non-hydrogen atoms were refined anisotropically. The hydrogen atoms in the crystal structures, except the lattice water molecules, were located from the difference Fourier maps and refined in the isotropic approximation. The hydrogen atoms of the lattice water molecules of compound **12** could not be located from the difference Fourier maps and are fixed at their normalized distances to obtain the hydrogen bonding patterns in the crystal structure. Because of the poor crystal qualities of compounds **10** and **11**, the thermal ellipsoids of the lattice water O atoms are comparatively larger and have a high degree of thermal motion. The structural diagrams were drawn with Diamond 3.2.[38] Data collection and refinement parameters for the complexes **10**, **11** and **12** are summarized in **Table 5.1**.

5.2.4 Theoretical methods

The energies of the geometries of the complexes included in this study were computed at the B3LYP-D/def2-TZVP level of theory using the crystallographic coordinates in the GAUSSIAN-09 program.[39] We also have used the Grimme's dispersion[40] correction as implemented in GAUSSIAN-09 program since it is adequate for the evaluation of non-covalent interactions where dispersion effects are relevant like in π-stacking interactions. The molecular electrostatic potential surface has been computed at the same level using Gaussian-09. The basis set superposition error for the calculation of interaction energies has been corrected using the counterpoise method.[41] The NCI plot[42] isosurfaces have been used to characterize non-covalent interactions. They correspond to both favourable and unfavourable interactions, as differentiated by the sign of the second density Hessian eigen value and defined by the isosurface colour. The colour scheme is a red-yellow-green-blue scale with red for ρ^{+}_{cut} (repulsive) and blue for ρ^{-}_{cut} (attractive).

5.2.5 Cell line and drug preparation

The *in vitro* cytotoxicity and apoptosis inducing abilities of the complexes **10**, **11** and **12** against Dalton's lymphoma (DL) malignant cancer cell lines were evaluated. The DL cells were cultured in RPMI-1640 medium supplemented with 10% FBS (Fetal Bovine Serum), gentamycin (20 mg/mL), streptomycin (100 mg/mL) and penicillin (100 IU) in a CO_2 incubator at 37°C with 5% CO_2; 80% confluent of exponentially growing cells were sub-cultured and used in the present study. The different doses (0, 0.01, 0.1, 0.5, 1, 5 and 10 μM) of the complexes **10**, **11** and **12** were prepared by dissolving in conditioned media (pH = 7.4).

5.2.6 MTT cell viability assay

Cell proliferations in terms of cell viability were determined by MTT assay in DL and peripheral blood mononuclear cells (PBMC) [normal cells] according to the

5.2.7 Crystal Data

Table 5.1 Crystal data and structure refinement data for **10**, **11** and **12**.

Crystal Parametres	**10**	**11**	**12**
Emprical formula	$C_{12}H_{12}CoN_2O_7$	$C_{12}H_{12}N_2NiO_7$	$C_{12}H_{14}CuN_2O_7$
Formula weight	355.17	354.95	361.79
Temperature (K)	293(2)	293(2)	293(2)
Wavelength (Å)	0.71073	0.71073	0.71073
Crystal system	Monoclinic	Monoclinic	Monoclinic
Space group	$P2_1/c$	$P2_1/c$	$P2_1/c$
a/Å	10.6062(7)	10.5818(4)	14.8466(7)
b/Å	20.1457(13)	20.0941(8)	13.4836(6)
c/Å	7.3306(5)	7.2854(3)	7.1539(3)
α °	90	90	90
β°	105.493(3)	105.089(3)	90.648(2)
γ °	90	90	90
Volume (Å^3)	1509.41(17)	1495.70(10)	1432.02(11)
Z	4	4	4
Calculated density (Mgm^{-3})	1.563	1.585	1.678
Absorption coefficient (mm^{-1})	1.172	1.332	1.562
F(000)	724	736	740
Crystal size (mm^3)	0.33 × 0.22 × 0.14	0.33 × 0.22 × 0.15	0.36 × 0.28 × 0.11
θ range for data collection(°)	1.99 to 28.54	1.99 to 27.13	1.37 to 25.00
Index ranges	-12<=h<=14, -27<=k<=16, -9<=l<=9	-13<=h<=12, -25<=k<=25, -9<=l<=9	-17<=h<=17, -15<=k<=16, -8<=l<=8
Reflections collected	21083	21748	16755
Refinement method	Full-matrix least squares on F^2	Full-matrix least-squares on F^2	Full-matrix least-squares on F^2
Data / restraints / parameters	3798 / 0 / 199	3299 / 0 / 199	2528 / 0 / 205
Goodness-of-fit on F^2	1.088	1.074	1.052
Final R indices [$I>2\sigma(I)$] $R1$/ $wR2$	0.0458/ 0.1450	0.0465/ 0.1440	0.0266/ 0.0729
R indices(all data) $R1$/ $wR2$	0.0619/ 0.1567	0.0631/ 0.1565	0.0300/ 0.0746
Largest diff. peak and hole (e.Å^{-3})	0.988 and -0.466	1.031 and -0.324	0.272 and -0.241

$wR2 = \{\Sigma [w(F_o^2 - F_c^2)^2] / \Sigma [w(F_o^2)^2] \}^{1/2}$; $R1 = \Sigma \mid |F_o| - |F_c| \mid / \Sigma |F_o$ $*GooF = S = \{\Sigma [w(F_o^2 - F_c^2)^2] / (n-p)$

instructions in the Cell Proliferation Kit.[43] As discussed in the previous chapters, multiple doses (0, 0.01, 0.1, 0.5, 1, 5 and 10 μM) of all the three complexes are incubated for 24 hours and then 10 µL of the MTT reagent (5 mg/mL in phosphate-buffered saline) was added into each well. The reaction mixture was then incubated for four hours under 5% CO_2 and 95% air at 37ºC. Following that, 100 µL of the DMSO was poured into each well and gently shaken.

5.2.8 Cell proliferation and apoptosis assay

A dual fluorescence based staining method involving acridine orange/ethidium bromide (AO/EB) is used to assess the rates of cell proliferation and apoptosis induction potential of the complexes **10**, **11** and **12**.[44] The procedure of apoptosis study has been discussed in detail in Chapter 2. Control and treated cancer cells were collected after 24 hours of treatment, washed with PBS (phosphate-buffered saline) and to the cell suspension; 20 μL of AO/EB dye mixture (100 μg/mL of each dye in distilled water) was added, mixed gently and incubated for 5 min in dark. The cells were thoroughly examined under fluorescence microscope and photographed. About 1000 cells were analyzed, and the percentage of apoptotic nuclei was counted for three independent determinations. The live cells produce green fluorescence, whereas apoptotic cells display condensed and fragmented orange to red fluorescence.[45]

5.2.9 Molecular docking

The results of MTT cell viability and apoptosis assays revealed the involvement of apoptotic cell death after treatment. In order to further corroborate the apoptosis cell death mechanism, molecular interactions between the complexes **10**, **11** and **12** and apoptotic regulator target protein, BCL-2 were studied by using Molegro Virtual Docker (MVD 2010.4.0) software.[46] As discussed in Chapter 2, the 3D coordinates of target protein BCL-2 (PDB ID: 2O22) were retrieved from Protein Data Bank (PDB).[47] The molecular arrangement and geometry of the compounds **10**, **11** and **12** were fully optimized using the semi-empirical quantum chemistry method (Parametric Method 3). The docking parameters were run using a GRID of 15 Å in radius and 0.30 in resolution with number of runs: 10 runs; algorithm: Moldock SE; maximum interactions: 1500; maximum population size: 50; maximum steps: 300; neighbour distance factor: 1.00; maximum number of poses returned: 5 to cover the ligand-biding site of the proteins structure.[48] Further, the analysis of protein-ligand complex binding site was analyzed and visualized by BIOVIA Discovery Studio (http://3dsbiovia.com/products/) and Chimera software (https://www.cgl.ucsf.edu/chimera/).[49]

5.2.10 Pharmacophore modelling

Ligandscout software is used as discussed in the previous chapters to generate the pharmacophore model of all the three complexes which demonstrated Structure Activity Relationship (SAR).[50] After performing molecular docking simulation, the best docking orientations (pose) were loaded into Ligandscout software and key pharmacophore features that include H-bond donor, H-bond acceptor, hydrophobic, aromatic, halogen bond donor, positive and negatively ionizable groups were identified.[50] Physicochemical properties, lipophilicity, water solubility, pharmacokinetics and drug likeness properties were predicted for the complexes using Swiss Target Prediction (http://www.swisstargetprediction.ch/). This server generates the most probable macromolecular targets of a small bioactive molecule and the prediction is based on the combination of 2D and 3D similarity with a library of 370'000 known actives on more than 3000 proteins.

5.2.11 Statistical analysis

Data are expressed as mean ± standard deviation (S.D.). To determine the significance of the differences among the groups, one-way ANOVA was performed followed by Post hoc test. $P \leq 0.05$ was considered to be statistically significant.

5.3 RESULTS AND DISCUSSION

5.3.1 Synthesis and general aspects

The complexes $[Co(py)(2,6\text{-}PDC)(H_2O)_2]\cdot H_2O$ (**10**), $[Ni(py)(2,6\text{-}PDC)(H_2O)_2]\cdot H_2O$ (**11**) and $[Cu(py)(2,6\text{-}PDC)(H_2O)]\cdot 2H_2O$ (**12**) have been isolated in high yield by reacting one equivalent of the respective metal chlorides, $MCl_2\cdot nH_2O$ with one equivalent of pyridine and one equivalent of disodium 2,6-pyridinedicarboxylate in water. Complexes **10**, **11** and **12** are moderately soluble in water; however, their solubility in common organic solvents is low. The complexes **10**, **11** and **12** show room temperature μ_{eff} values of 3.87 BM, 2.81 BM and 1.74 BM respectively and confirm the presence of three, two and one unpaired electrons per metal centers.[51]

5.3.2 Spectral Properties

5.3.2.1 FT-IR Spectroscopy

FT-IR spectra of the complexes **10**, **11** and **12** (KBr pellets) were recorded in the region 4000-500 cm^{-1} (**Figure 5.1**). The bands have been tentatively assigned on the basis of reported literature.[52] Being isostructural, the complexes **10** and **11** are found to have similar and very close peaks. The peaks for the symmetric and anti-symmetric ν(OH) stretching vibrations of coordinated and/or lattice water molecules are obtained at expected positions (3210-3400 cm^{-1}) as described in previous chapters.[53] The broad peak at around 3074 cm^{-1} for all the three complexes can be attributed to the C−H stretching vibrations of the coordinated *py* ring.[54] Tamer *et al*. have reported the C−H stretching vibrations of the coordinated *py* ring at 3136-3064 cm^{-1} for pyridine-2-carboxylic acid and its two derivates, 4-methoxy-pyridine-2-carboxylate and 4-chloro-pyridine-2-carboxylate.[55]

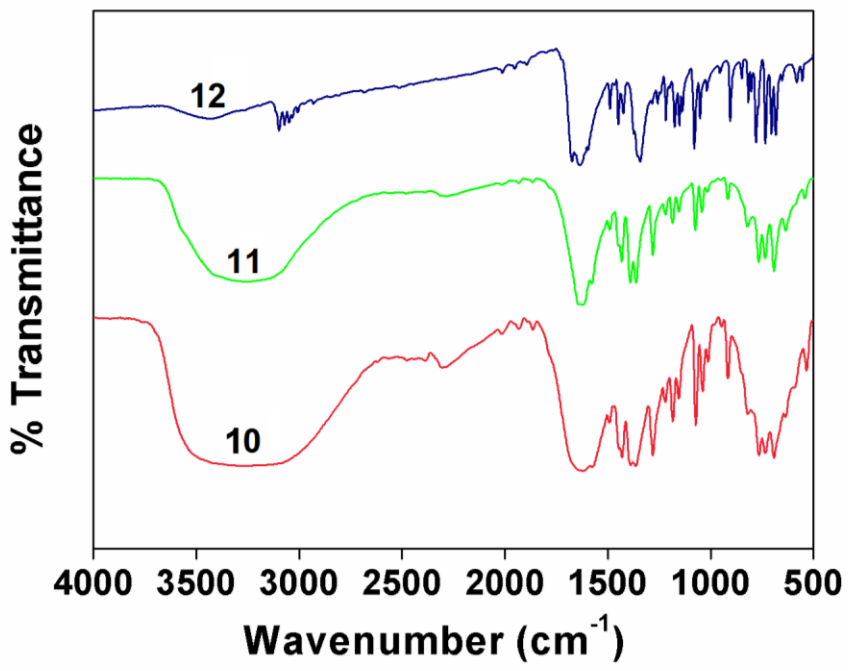

Figure 5.1 FT-IR spectra of the complexes **10**, **11** and **12**.

The absence of the bands at around 1710 cm^{-1} for compounds **10**, **11** and **12** indicates that the carboxyl groups of *2,6-PDC* get completely deprotonated to the respective anion upon coordination with the metal ions.[56] Burak and his research group also reported the absence of the same band which reveals deprotonation of carboxyl group of *2,6-PDC* in $(H_2pip)_n[Ln_2(2,6\text{-}PDC)_4(H_2O)_2]_n$ [Ln = La and Nd, H_2pip = piperazine].[57] The differences (Δν) between ν_{as}(OCO) and ν_s(OCO) vibrational frequencies of carboxylate groups of *2,6-PDC* are found to be 258 cm^{-1}, 233 cm^{-1} and 286 cm^{-1} for **10**, **11** and **12** respectively, which indicate the monodentate coordination of the carboxylate moiety of *2,6-PDC* to the respective metal centers.[58] Shams *et al.* have also found similar difference (Δν) that is greater than 200 cm^{-1} for substituted *2,6-PDC* complex *viz.* (Hdap)[VO_2(hp2,6-PDC)] [where, hp2,6-PDC = 4-hydroxypyridine-2,6-dicarboxylate and dap = 3,4-diaminopyridine] supporting the monodentate coordination of the carboxylate moiety.[59] In the spectra of all the three complexes, bands between 900 and 1217 cm^{-1} can be attributed to the coordinated *py* to the metal centers.[60] These observations are well consistent with the structures as determined by the single crystal XRD analysis.

5.3.2.2 Electronic Spectroscopy

The electronic spectra of compound **10** in the solid and aqueous phases are shown in **Figure 5.2(a)** and **5.2(b)** respectively. The aromatic ligands in the UV-Vis-NIR spectrum exhibit absorption bands in the UV region at around 288 nm which is assigned to the intra ligand n→π* transition.[61] Complex **10** in the solid state exhibits two distinct absorption bands at 1151 nm and 480 nm which can be assigned to $^4T_{1g}(F)\rightarrow{}^4T_{2g}(F)$ (ν_1) and $^4T_{1g}(F)\rightarrow{}^4T_{1g}(P)$ (ν_3) transitions respectively. However, the ν_2 band due to $^4T_{1g}(F)\rightarrow{}^4A_{2g}(F)$ transition appears at 515 nm with a shoulder at 635 nm because of a two-electron transition.[54] In the aqueous state, the weak absorption band at 461 nm can be assigned to $^4T_{1g}(F)\rightarrow{}^4T_{1g}(P)$ (ν_3) transition. The ν_2 band at 503 nm [$^4T_{1g}(F)\rightarrow{}^4A_{2g}(F)$ (ν_2)] splits into two in the aqueous phase with a shoulder at 578 nm due to two electron transition. As observed in the solid state, absorption band for n→π* transition in aqueous phase is obtained at 307 nm.

The bands observed due to d-d electronic transitions suggest the octahedral environment of **10** around the Co(II) centre in both the phases.[62] Three similar ligand field bands are also observed in a recent report of Akinyele and his research group for an octahedral Co(II) complex *viz.* [Co(ASA)L(H_2O)Cl] [where, L = m-hydroxylbenzaldehyde-4-nitrobenzoylhydrazone; ASA = aspirin].[63]

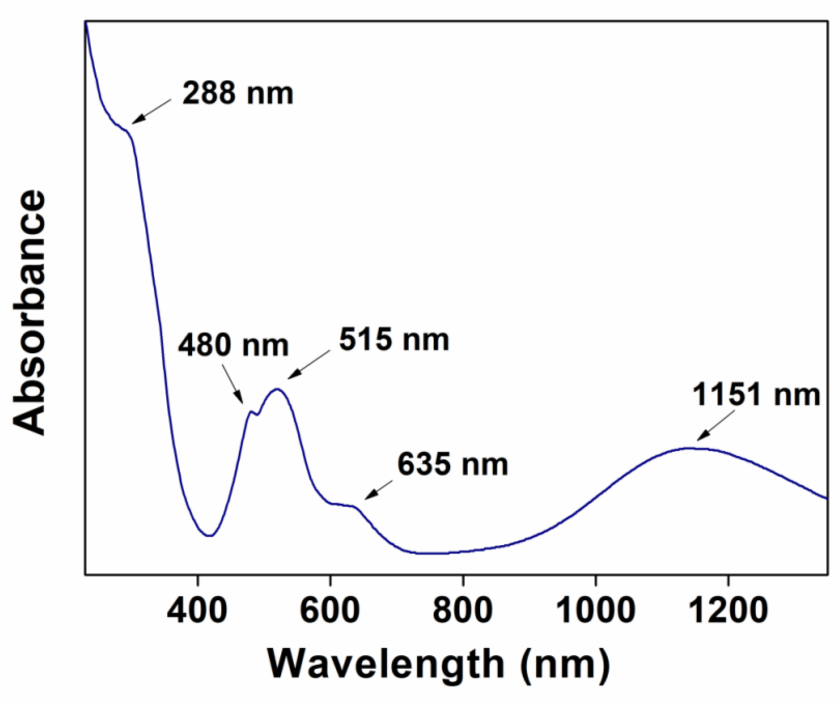

(**a**)

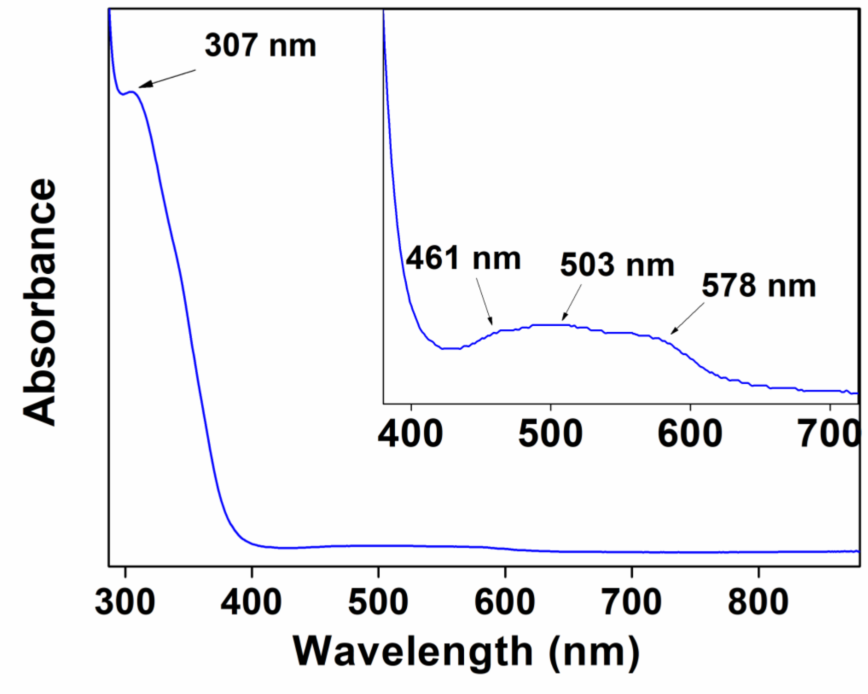

(**b**)

Figure 5.2(**a**) UV-Vis-NIR spectrum of [Co(py)(2,6-PDC)(H_2O)$_2$]·H_2O (**10**); (**b**) UV-Vis spectrum of [Co(py)(2,6-PDC)(H_2O)$_2$]·H_2O (**10**) in water.

The UV-Vis-NIR spectrum of complex **11** [**Figure 5.3(a)**] shows three ligand field bands at 1079, 615 and 390 nm, associated with the spin allowed transitions from the $^3A_{2g}$ ground state to the three excited triplet states, *viz*. $^3T_{2g}$(F), $^3T_{1g}$(F) and $^3T_{1g}$(P) respectively.[64] The first spin-allowed transition to the $^3T_{2g}$(F) state occurs at 1079 nm for complex **11**. The $^3A_{2g}\rightarrow^3T_{1g}$(F) transition ($\nu_2$) at around 615 nm shows a shoulder at 745 nm which may be a consequence of the transition from the $^3A_{2g}$(F) to ^1E_g level, gaining intensity through a configuration interaction with the $^3T_{1g}$(F) level, although some investigators prefer to interpret the doublet as arising from spin-orbit coupling.[65] The peak observed at 390 nm is due to the $^3A_{2g}\rightarrow^3T_{1g}$(P) transition. The absorption peak at 256 nm can be assigned to the n→π* absorption of aromatic ligands, whereas the shoulder at around 361 nm is attributed to the LMCT (ligand to metal charge transfer) transition.[61]

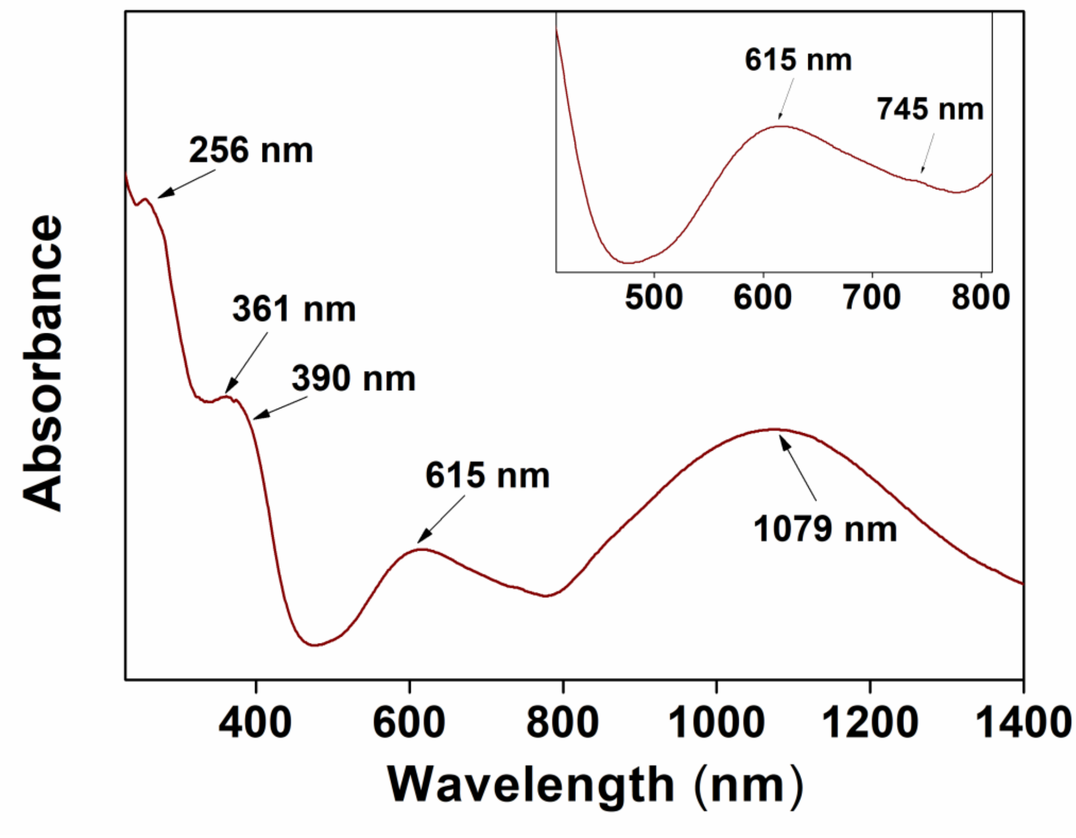

(a)

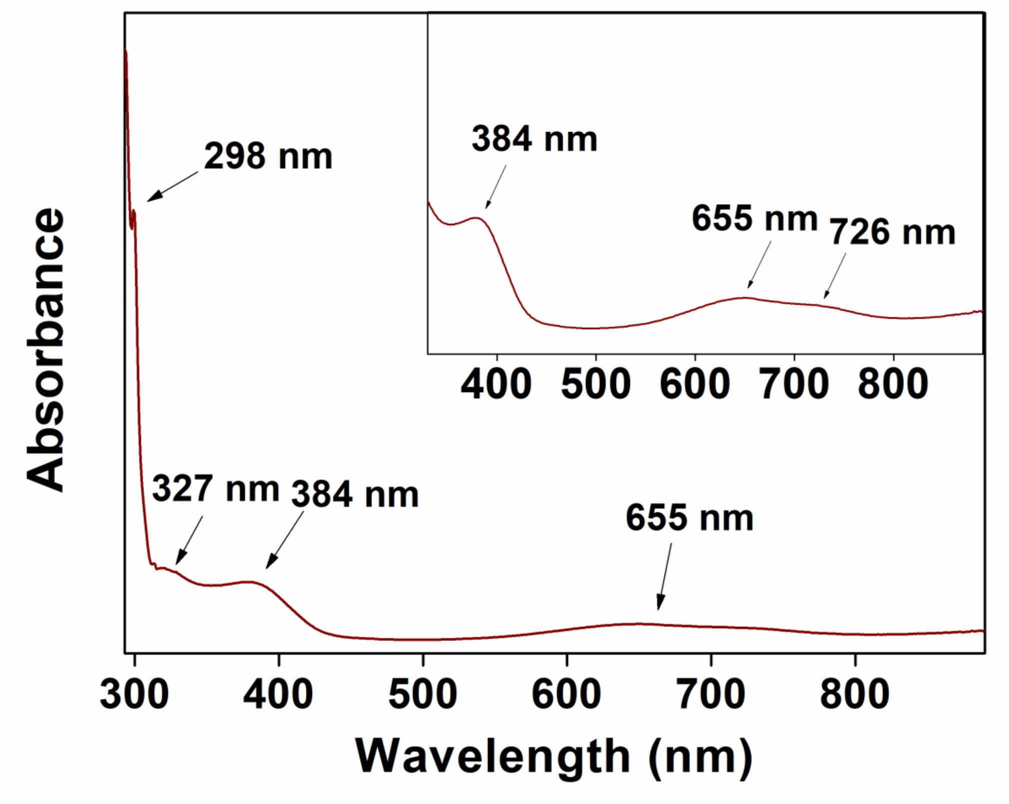

(**b**)

Figure 5.3(**a**) UV-Vis-NIR spectrum of [Ni(py)(2,6-PDC)$(H_2O)_2$]·H_2O (**11**); (**b**) UV-Vis spectrum of [Ni(py)(2,6-PDC)$(H_2O)_2$]·H_2O (**11**) in water.

The UV-Vis spectrum [**Figure 5.3**(**b**)] of **11** in water exhibits absorption band at 298 nm for the intra ligand n→π* transition, whereas peaks at around 327 nm is attributed to the LMCT (ligand to metal charge transfer) transition. The absorption band at 384 nm can be assigned to $^3A_{2g}(F)\rightarrow{}^3T_{2g}(F)$ transition for octahedral Ni(II) ions. Similar splitting of the band for the aqueous phase spectrum at 655 nm for $^3A_{2g}(F)\rightarrow{}^3T_{1g}(P)$ transition is also observed with a shoulder at around 726 nm. Electronic spectra of recently reported octahedral Ni(II) coordination complexes *viz.* [Ni(tcnz)$_2$(NO_3)$_2$].H_2O, [Ni(tcnz)$_2$(OAc)$_2$]$_2$.3H_2O, [Ni(tcnz)$_3$$Br_2$($H_2O$)], [Ni(tcnz)$_6$]$Cl_2$ and [Ni(tcnz)$_6$]Br_2 [where, tcnz = tioconazole] resemble the spectral bands observed in the solid and in aqueous phases of complex **11**.[66]

The UV-Vis-NIR spectrum of compound **12** indicates the distortion of Cu(II) coordination in the complex from O_h symmetry [**Figure 5.4**(**a**)]. The broad band due to the d-d transition splits into two, giving bands at 674 nm and 947 nm, suggesting distorted square-pyramidal copper centre which agrees with the single crystal X-ray structure.[67] The UV-Vis spectrum of complex **12** was also recorded in water [**Figure 5.4(b)**]. An octahedral or a square-pyramidal copper(II) complex in the aqueous phase is expected to show one broad absorption band in the electronic spectrum due to t_2 to e transition in the visible region.[61] In complex **12**, a broad absorption band is observed at 686 nm that is typical of those associated with d-d transitions in square-pyramidal Cu^{2+} complexes.[68] The observed electronic spectral bands are in good agreement with the literature observed for the complexes of types; $[Cu(py)_2(pfb)_2(H_2O)]$ [where, py = pyridine and pfb = pentafluorobenzoate] and $\{[Cu(\mu\text{-}O,O'\text{-}SO_4)(Hdmpz)_2(H_2O)]\cdot 2H_2O\}_n$ [where, Hdmpz = 3,5-dimethylpyrazole].[68] The n→π* band for the complex **12** in both the phases is found in the expected positions. The NIR band is not seen in the solution spectra of the complexes **10** and **11** because of the limit in the wavelength window of the spectrophotometer used.[69]

The electronic spectral studies reveal that the complexes **10**, **11** and **12** do not show marked differences in the position of the absorption peaks in the solid and in the aqueous phases. Therefore, it may be assumed that the bonding modes as well as the geometries of the synthesized complexes do not change in the solution phase.[70]

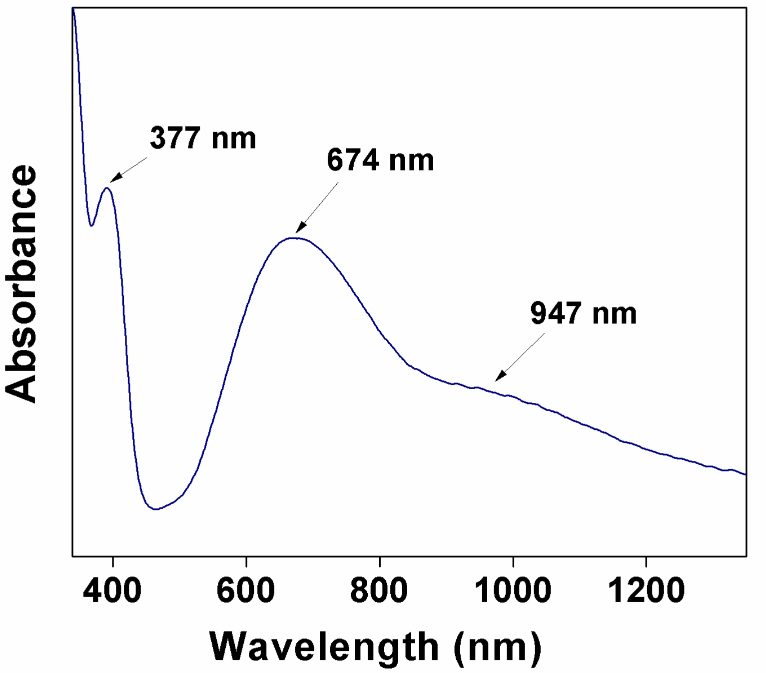

(a)

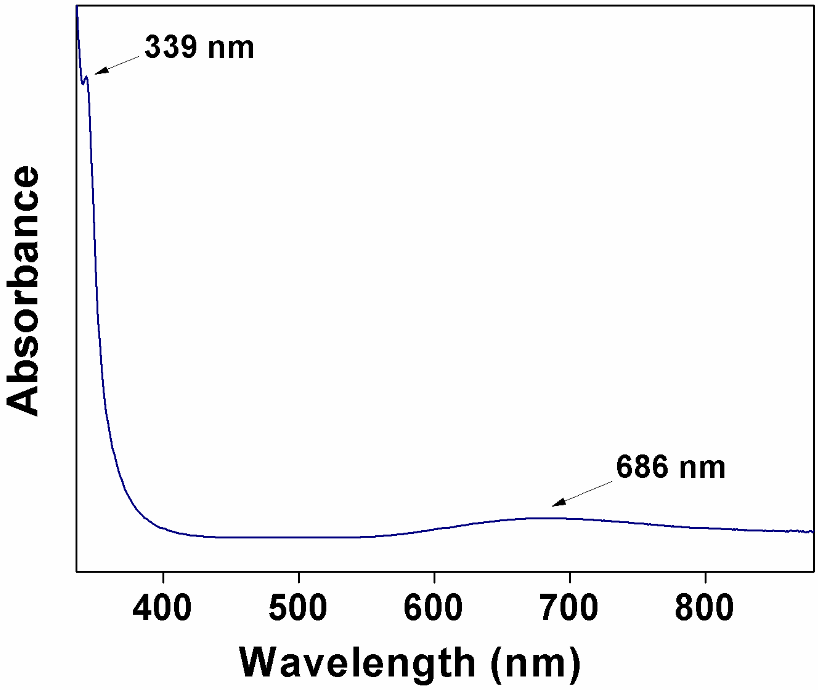

(**b**)

Figure 5.4(**a**) UV-Vis-NIR spectrum of [Cu(py)(2,6-PDC)(H_2O)$_2$]·2H_2O (**12**); (**b**) UV-Vis spectrum of [Cu(py)(2,6-PDC)(H_2O)$_2$]·2H_2O (**12**) in water.

5.3.3 Crystal structures

5.3.3.1 Crystal structures of [Co(py)(2,6-PDC)(H_2O)$_2$]·H_2O (10) and [Ni(py)(2,6-PDC)(H_2O)$_2$]·H_2O (11)

Single-crystal X-ray diffraction analysis reveals that complexes **10** (**Figure** 5.5) and **11** (**Figure** 5.6) are a pair of isostructural complexes, and crystallize in the monoclinic system with space group $P2_1/c$. Therefore, only the structure of compound **10** is described here in detail as a representation.

As shown in **Figure** 5.5(**a**), one Co(II), one doubly deprotonated tridentate chelating *2,6-PDC* ligand, one pyridine molecule, two coordinated and one lattice water lie in the asymmetric unit of **10**. The thermal ellipsoids of the lattice water O atom is comparatively larger than the rest for compound **10** and have a high degree of thermal motion. The crystallographically independent Co(II) is six-coordinated with two nitrogen atoms (N1 and N2) from *py* and *2,6-PDC* and four oxygen atoms (O1, O2, O3 and O5) from two aqua ligands and *2,6-PDC* moiety, resulting in a distorted octahedral geometry. The equatorial plane of **10** is defined by O3 and O5 of *2,6-PDC*, and two coordinated aqua (O1 and O2) ligands. N1 and N2, from *py* and *2,6-PDC* respectively, are positioned at the axial sites with a bond angle of 174.270(3)°. The sum of the bond angles of O1–Co1–O3 [87.924(2)°], O3–Co1–O2 [86.477(2)°], O2–Co1–O5 [91.518(2)°] and O5–Co1–O1 [95.996(2)°] is 361.915°, showing that O1, O2, O3, and O5 atoms are coplanar (mean r.m.s. deviation of 0.3024 Å and 0.2597 Å respectively for **10** and **11**). A comparative study shows that the average Co–O, Co–N and Ni–O, Ni–N bond lengths are almost consistent with the previously reported Co(II) and Ni(II) complexes.[51, 69] Selected bond lengths and angles for **10**, **11** and **12** are listed in **Table 5.2**.

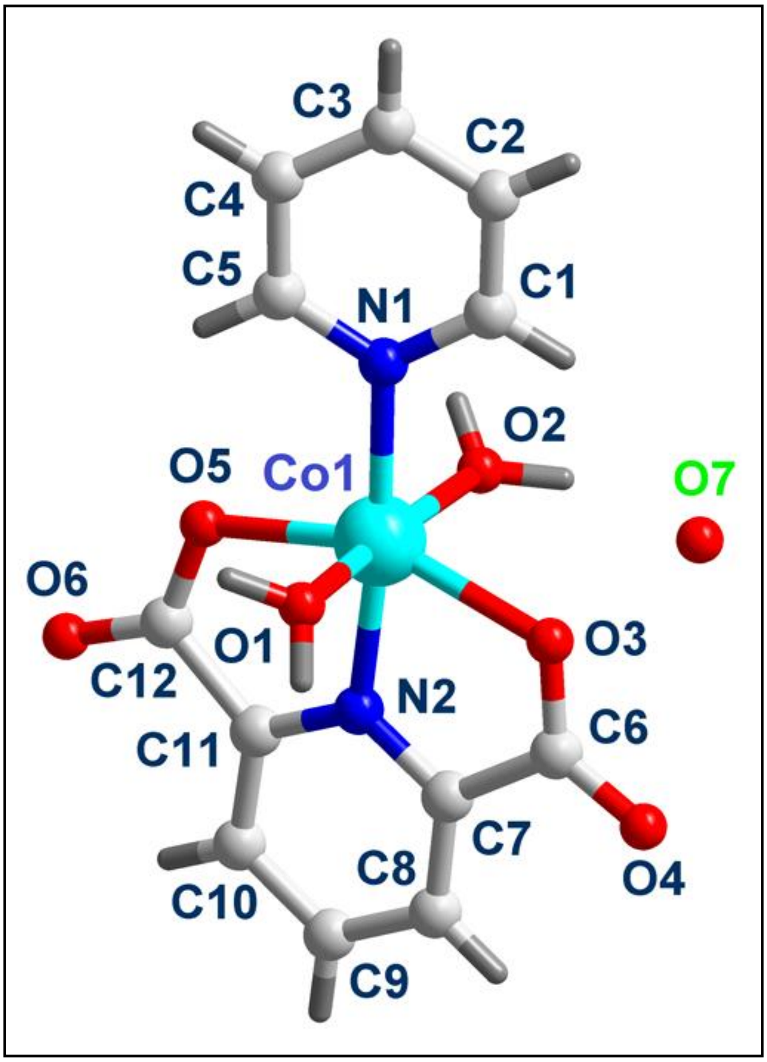

Figure 5.5 Molecular structure of [Co(py)(2,6-PDC)(H_2O)$_2$]·H_2O (**10**).

Table 5.2 Selected bond lengths (Å) and bond angles (°) for **10**, **11** and **12**.

Bond length	**10**	**11**	**12**	
M–O1	2.102(2)	2.084(3)	Cu1–O1	2.308(2)
M–O2	2.109(2)	2.095(3)	Cu1–O6	2.039(2)
M–O3	2.179(2)	2.162(2)	Cu1–O5	2.013(2)
M–O5	2.178(2)	2.132(2)	Cu1–N1	1.962(2)
M–N1	2.095(2)	2.045(3)	Cu1–N2	1.903(2)
M–N2	2.048(2)	1.990(3)		
Bond angle	**10**	**11**	**12**	
N1–M–O2	88.61(8)	89.52(1)	N1–Cu1–N2	173.52(8)
N1–M–O3	110.27(8)	105.87(1)	N1–Cu1–O1	92.74(8)
N1–M–N2	174.31(9)	177.16(1)	N1–Cu1–O6	97.65(7)
N1–M–O5	98.10(9)	99.08(1)	N1–Cu1–O5	100.32(7)
N1–M–O1	88.22(8)	87.67(10)	N2–Cu1–O1	93.50(7)
O2–M–O3	86.51(7)	88.28(8)	N2–Cu1–O6	80.24(7)
O2–M–N2	92.10(8)	90.87(9)	N2–Cu1–O5	81.00(7)
O2–M–O5	91.47(8)	90.80(9)	O1–Cu1–O6	93.29(7)
O2–M–O1	172.23(8)	174.14(9)	O1–Cu1–O5	93.96(7)
O3–M–N2	75.41(8)	76.92(9)	O5–Cu1–O6	160.25(7)
O3–M–O5	151.48(7)	155.0(8)		
O3–M–O1	87.94(7)	87.533(8)		
N2–M–O5	76.24(8)	78.13(8)		
N2–M–O1	91.76(8)	92.18(9)		
O5–M–O1	96.00(8)	94.72(8)		

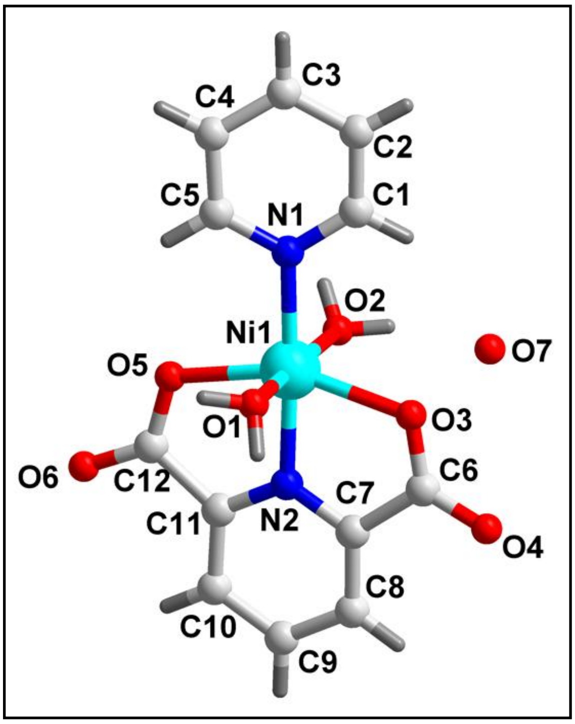

Figure 5.6 Molecular structure of $[Ni(py)(2,6\text{-}PDC)(H_2O)_2]\cdot H_2O$ (**11**).

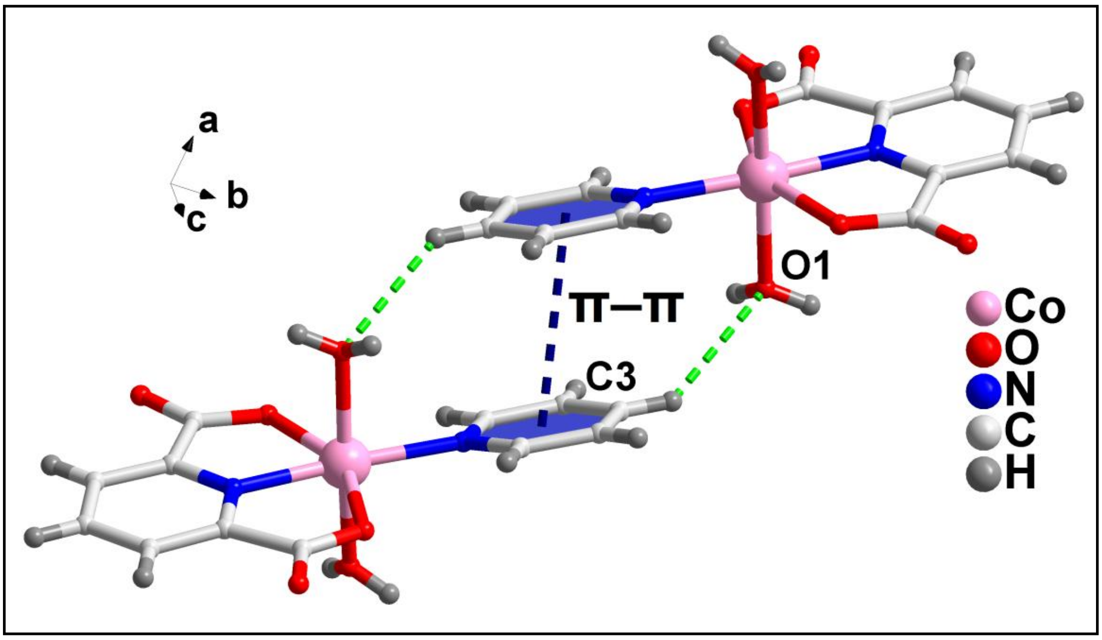

(**a**)

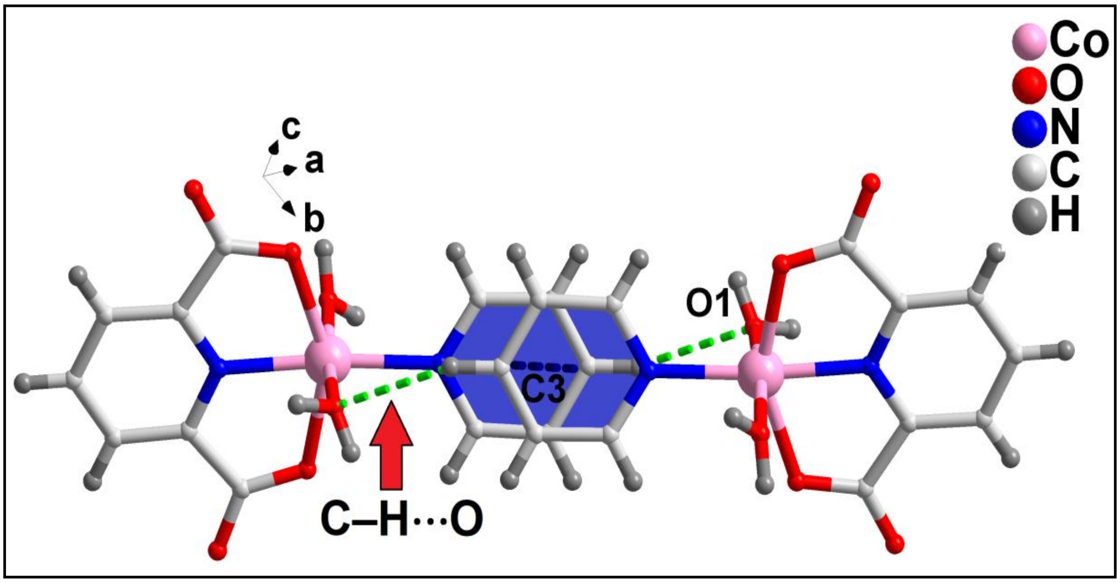

(**b**)

Figure 5.7 Formation of supramolecular dimers in the crystal structure of [Co(py)(2,6-PDC)(H_2O)$_2$]·H_2O (**10**); (**a**) π-stacked dimers, (**b**) on-top representation of the dimer involving C–H···O and π-stacking interactions.

Anti-parallel π-stacking and symmetrically equivalent C–H···O hydrogen bonding interactions (**Figure 5.7**) are observed in the supramolecular dimer of compound **10**. The anti-parallel π-stacking interaction occurs between two aromatic rings of *py* from adjacent monomeric units with centroid(N1, C1-C5)···centroid(N1, C1-C5) separation of 3.643 Å. Symmetrically equivalent C–H···O hydrogen bonding interactions are also observed, that involve the coordinated water molecules (O1) with C3–H3···O1 distance of 2.715 Å. Theoretical studies have been performed (*vide infra*) on the supramolecular dimer to analyse the anti-parallel π-stacking interaction in complex **10**.

Strong O–H···O and C–H···O hydrogen bonds along with non-covalent l.p···π interactions are involved in the formation of 1D supramolecular chain along *a*-axis in the crystal structure of **10** (**Table 5.3**). The neighbouring monomeric units of **10** are interconnected by strong O–H···O hydrogen bond at donor(O5)–acceptor(O2) distance of 2.725 Å, involving the coordinated carboxylic O5 atom of *2,6-PDC* and the coordinated aqua ligand (O2) to produce a supramolecular dimer (**Figure 5.8**). This dimer is further stabilized by C–H···O and C=O(l.p.)···π interactions. C5H5 moiety of the coordinated *py* ligand of one monomeric unit and the coordinated aqua ligand (O2) of the adjacent monomeric unit are involved in C–H···O hydrogen bonds with C5–H5···O2 = 2.854(2) Å. Similarly, the C2–H2 moiety of the coordinated *py* ligand of one unit is involved in another C–H···O interaction with the non-coordinated carboxylic O atoms (O6) of *2,6-PDC*, having distance of C2–H2···O6 = 2.570 Å.

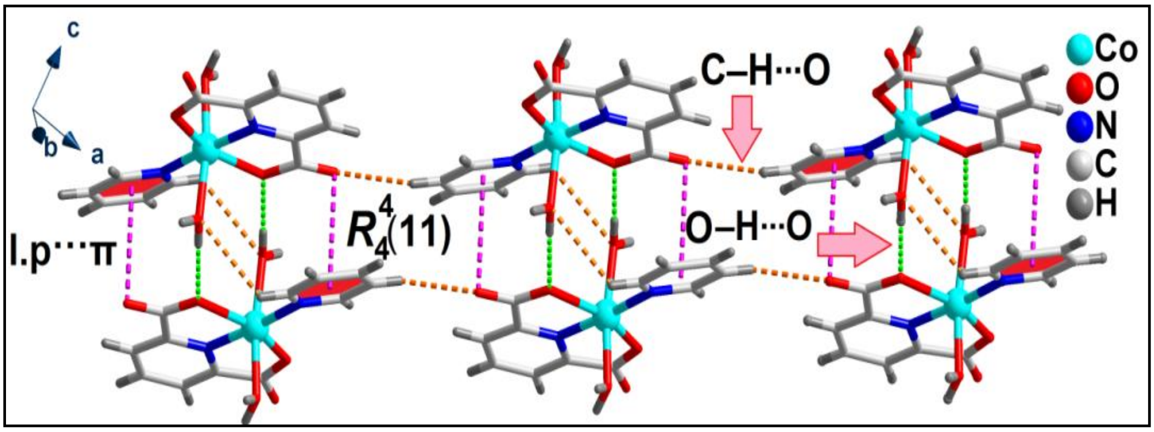

Figure 5.8 Hydrogen-bonded 1D double-chain of [Co(py)(2,6-PDC)$(H_2O)_2$]·H_2O (**10**) along *a*-axis.

Within this dimer, C=O(l.p.)···π interactions observed between C=O moiety (O6) of *2,6-PDC* and the π-system of *py* ligand have a separation of 3.476 Å between the carboxylate oxygen O6 (which is also involved in C–H···O bonds; **Table 5.3**) and the centroid of the *py* ring.[71] The angle between the oxygen (O6), the ring centroid and the aromatic plane is 94.12(2)°.[72] Biswas *et al*. have reported (l.p.)···π interactions involving carboxylate C=O moiety in $[Cu_2(pic)_3(Hbyp)(H_2O)(ClO_4)_2]$ [where, pic = picolinate, Hbyp = 4,4′-bipyridine] with a similar separation of 3.24 Å.[73] An eleven-membered supramolecular ring motif having Etter[74] graph-set notation of $R_4^4(11)$ is formed (**Figure 5.8**) in the 1D supramolecular chain of **10** involving four monomeric units.

Two adjacent 1D chains of **10** are interconnected through various non-covalent supramolecular interactions including strong hydrogen bonding, weak C–H···C contacts and anti-parallel π-stacking interactions to produce 2D supramolecular network architecture along the *bc* plane (**Figure 5.9**). Strong O–H···O hydrogen bonds [O1–H1A···O4 = 1.927 Å and O2–H2A···O4 = 1.852 Å] assisted by coordinated aqua ligands from one chain and the non-coordinated carboxylic O atom of *2,6-PDC* from the adjacent chain are observed in the crystal structure. C–H···C contacts provide additional reinforcements within this layered architecture of **10**. The pairwise alignment of *2,6-PDC* molecules results in one pyridyl-H donor atom of one molecule apparently interacting with the carbon acceptor atom of the other with the distances of C(8)–H(8)···C(10) = 3.465(3) Å [$C(sp^2)$–H···$C(sp^2)$, C(8)–C(10) = 3.763 Å] and C(9)–H(9)···C(9) = 3.472(4) Å [$C(sp^2)$–H···$C(sp^2)$, C(9)–C(9) = 3.771 Å].[75] Furthermore, anti-parallel π–π interaction is observed between the monomeric units of **10**. Two anti-parallel aromatic rings of *py* from adjacent monomeric units are involved in π–π interaction with centroid···centroid separation of 3.644 Å. Bazargan and coworkers have reported similar antiparallel π–π interaction with centroid···centroid separation of 3.84 Å in the complex, $(Hamacr)_3[Fe(H_22,6\text{-}PDC)_3]\cdot 6H_2O$ [where, $H_22,6$-PDC = pyridine-2,6-dicarboxylate N-oxide and Hamacr = 9-aminoacridine].[76] The characteristics of this electrostatic π–π interaction are further investigated theoretically (*vide infra*) which justify the role of anti-parallel π–π interactions in stabilizing the 2D network structure of **10**.

The adjacent layered subunits further stack to give rise to an interesting 3D supramolecular framework with 1D channels (**Figure 5.10**) along the *c*-axis enclathrated by lattice water molecules (**Figure 5.11**).

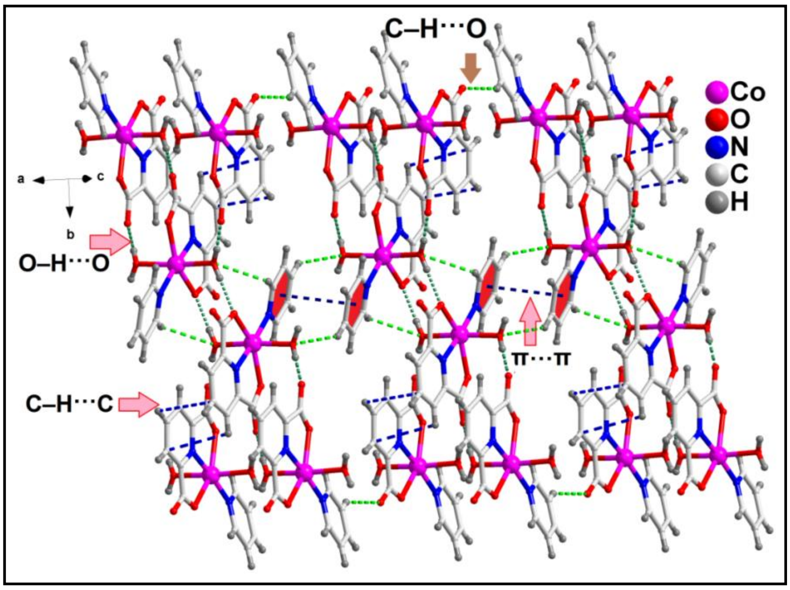

Figure 5.9 Formation of supramolecular layered assembly of [Co(py)(2,6-PDC)(H_2O)$_2$]·H_2O (**10**) along the *bc* plane assisted by anti-parallel π···π, O–H···O, C–H···O and unusual C–H···C contacts. Interactions between two adjacent 1D double-chains are only shown.

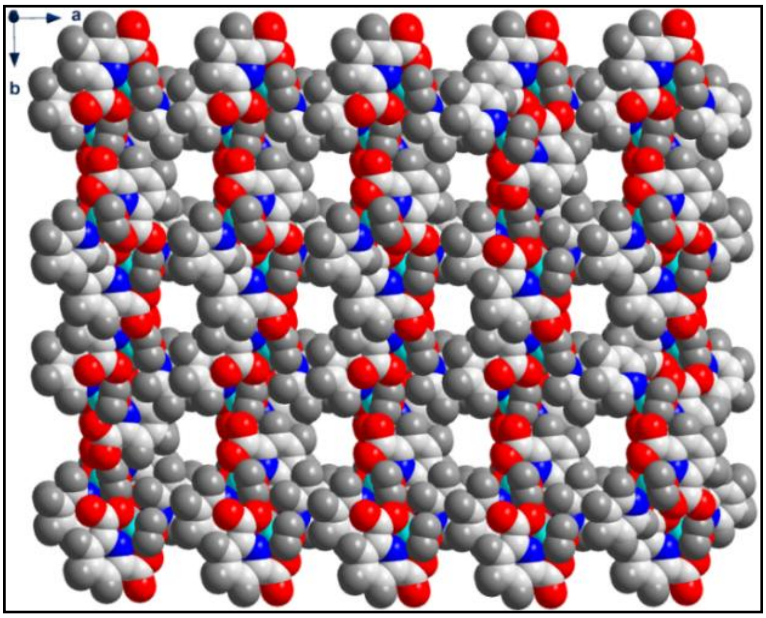

Figure 5.10 A perspective view of the 3D network of [Co(py)(2,6-PDC)(H_2O)$_2$]·H_2O (**10**) showing 1D open channels.

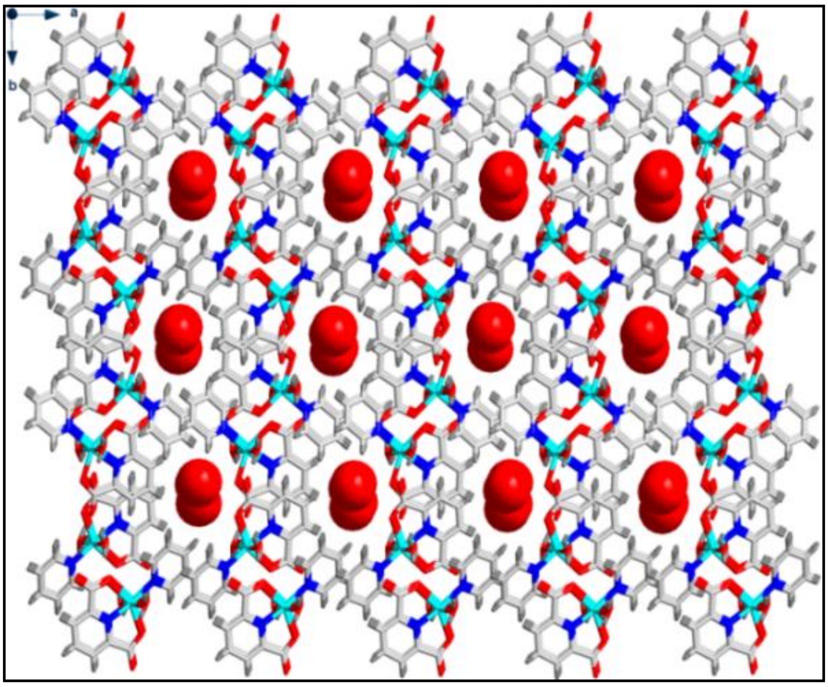

Figure 5.11 A perspective view of the 3D network of [Co(py)(2,6-PDC)(H_2O)$_2$]·H_2O (**10**) showing the enclathration of the lattice H_2O molecules (shown in space-filling model) within the 1D channels.

Table 5.3 Hydrogen bonding parameters (Å and °) of **10** and **11**.

D–H···A		d(D–H)	d(D–A)	d(H···A)	<(DHA)	Symmetry
O1–H1A···O4	**1**	0.8251	2.7483	1.9267 (20)	173.628 (149)	x, –y+1/2,+z+1/2
	2	0.8554	2.7346	1.8792 (22)	178.991 (155)	x, –y+1/2,+z+1/2
O1–H1B···O6	**1**	0.8531	2.6814	1.8338 (21)	171.998 (141)	–x+1, –y, –z+1
	2	0.8361	2.6818	1.8712 (25)	122.978 (160)	–x+1, –y, –z+2
O2–H2A···O4	**1**	0.8876	2.7379	1.8518 (20)	175.882 (133)	x, –y+1/2,+z–1/2
	2	0.8128	2.7677	1.9552 (22)	177.972 (161)	x, –y+1/2,+z–1/2
O2–O2B···O5	**1**	0.8171	2.7140	1.9077 (19)	178.087 (131)	–x+1, –y, –z
	2	0.8381	2.7400	1.9306 (22)	162.022 (154)	–x+1, –y, –z+1
C1–H1···O7	**1**	0.9291	3.585	2.8018 (96)	142.729 (276)	x,y,z
	2	0.9306	3.6052	2.9647 (16)	127.244 (388)	x,y,z
C8–H8···O2	**1**	0.9295	3.4689	2.7068 (19)	139.773 (192)	x, –y+1/2,+z+1/2
	2	0.9293	3.3841	2.6202 (27)	139.866 (244)	x, –y+1/2,+z+1/2
C8–H8···C10	**1**	0.9295	3.7679	3.4654 (33)	101.588 (190)	
	2	0.9293	3.7281	3.4235 (42)	101.925 (222)	
C9–H9···C9	**1**	0.9298	3.7706	3.4723 (39)	101.575 (222)	
	2	0.9298	3.7459	3.9985 (43)	67.708 (217)	

5.3.3.2 Crystal structure of [Cu(py)(2,6-PDC)(H_2O)]·2H_2O (12)

The single-crystal X-ray diffraction analysis reveals that complex **12** crystallizes in the monoclinic space group $P2_1/c$. The asymmetric unit of complex **12** consists of one copper atom, one *py* molecule, one *2,6-PDC*, one coordinated aqua ligand and two lattice water molecules. As illustrated in **Figure 5.12**, the crystallographically independent Cu1 di-positive ion is penta-coordinated by two nitrogen atoms (N1 and N2) and three oxygen atoms (O1, O5 and O6). The coordination geometry around Cu1 in **12** is slightly distorted square-pyramidal as evidenced by the value of the trigonality index $\tau = 0.22$[77], where the basal plane is formed by the O5, O6, N1, and N2 atoms (mean r.m.s. deviation of 0.0104 Å), while the apical position is occupied by the O1 atom. Dehghanpour *et al*. have reported the similar trigonality index value ($\tau = 0.22$ and 0.21) for a distorted square-pyramidal dinuclear Cu(II) complex for the metal centers.[78] The extent of distortion from the square-pyramid geometry is also reflected in the angles inside the coordination CuN_2O_3 chromophore. The angles formed by the atoms in *trans*-positions slightly deviate from 180° [O5–Cu1–O6 160.25(7)°, N1–Cu1–N2 173.51 (8)°], while the angles formed by the atoms in *cis*-positions fall within the range of 80.24(7)°–100.31(7)°. In addition, the apical Cu1–O1 bond length [2.307(2) Å] is much longer than the basal bonds. The average Cu–O and Cu–N bond distances are almost consistent with the previously reported square-pyramidal Cu(II) complexes.[72]

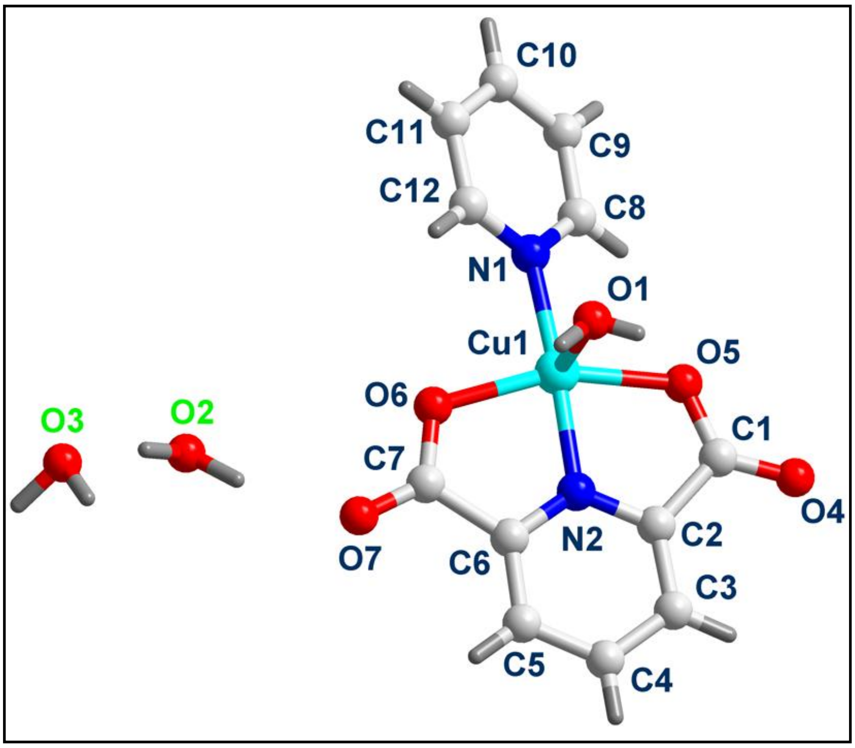

Figure 5.12 Molecular structure of $[Cu(py)(2,6\text{-}PDC)(H_2O)]\cdot 2H_2O$ (**12**).

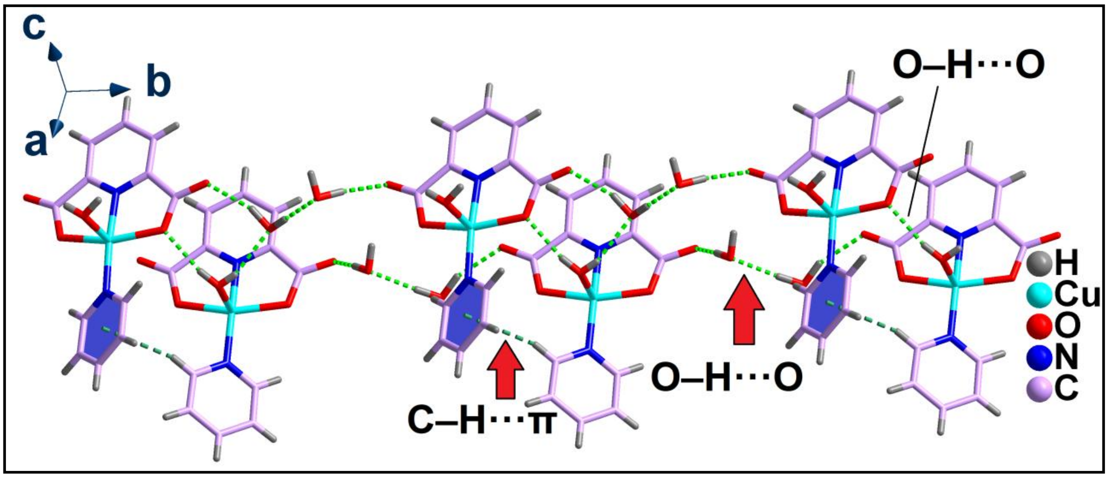

Figure 5.13 1D supramolecular chain between the monomeric units of [Cu(py)(2,6-PDC)(H_2O)]·$2H_2O$ (**12**) along *b*-direction.

In the crystal structure of **12**, strong O–H···O hydrogen bonding and C–H···π interactions are involved in the formation of a 1D supramolecular chain along *b*-direction (**Figure 5.13**). The non-coordinated carboxylate oxygen atom (O4) is involved in O–H···O hydrogen bonding with the lattice water molecule with O3–H3A···O4 distance of 1.956 Å. Similarly, coordinated aqua ligands are involved in hydrogen bonding with coordinated carboxylate oxygen atoms (O6) and lattice water molecule (O2) with distances O1–H1A···O6 = 1.997 Å, O1–H1B···O2 = 2.064 Å. Within the chain, the orientation of the coordinated pyridine ligands is such that the C12–H12 moiety of one ligand points toward the pyridyl π–cloud centroid of an adjacent one to give C–H···π interaction with hydrogen to centroid separation of 2.954 Å (**Figure 5.13**).

The 1D chains of **12** are interconnected through a number of supramolecular interactions to give a layered architecture in the *ab* plane (**Figure 5.14**). The uncoordinated oxygen atom of *2,6-PDC* is involved in C–H···O hydrogen bonding interaction with the –CH moiety of neighbouring *2,6-PDC* having H···O distance of 2.436 Å. Similar to **10**, weak C–H···C interactions are observed in the layered architecture of complex **12**, which play a crucial role in the stabilization of the architecture. –CH groups of *py* moiety of one Cu(II) unit are involved in several C–H···C contacts with the carbon atoms of the same moieties of the neighbouring monomeric units, having distances C12–H12···C12 = 3.157 Å, [C(sp^2)–H···C(sp^2), C(12)–C(12) = 3.962 Å]; C12–H12···C11 = 3.038 Å, [C(sp^2)–H···C(sp^2), C(11)–C(12) = 3.695 Å]; C11–H11···C11 = 3.967 Å [C(sp^2)–H···C(sp^2), C(11)–C(11) = 3.932 Å].

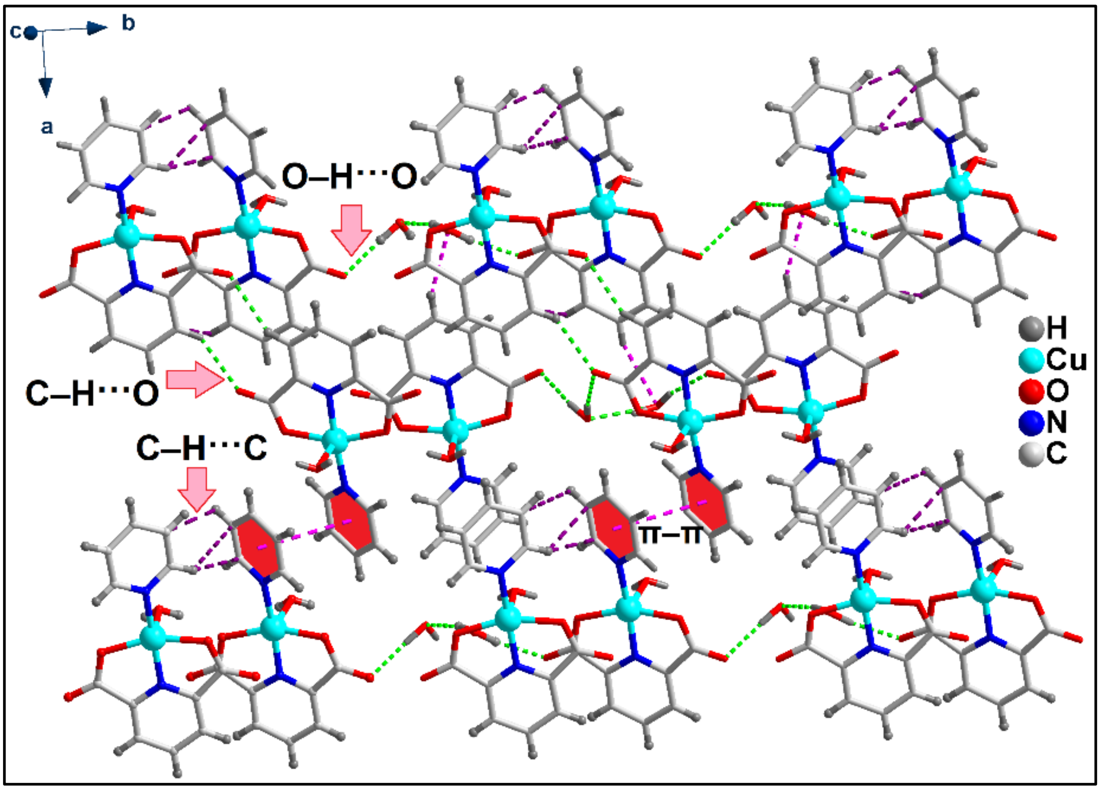

Figure 5.14 Formation of supramolecular layered assembly of [Cu(py)(2,6-PDC)(H_2O)]·$2H_2O$ (**12**) along *ab* plane assisted by anti-parallel π···π, C–H···O and unusual C–H···C contacts. Interactions between two adjacent 1D double-chains are only shown.

Similar to complex **10**, anti-parallel π-stacking interactions (**Figure 5.15**) are also observed in the crystal structure of **12** that occur between two anti-parallel aromatic rings of *py* from adjacent monomeric units with centroid···centroid separation of 3.684 Å. Two symmetrically equivalent C–H···O hydrogen bonding interactions are also observed in the dimer having C9–H9···O1 and C10–H10···O5 distances of 2.594 Å and 2.776 Å respectively. Theoretical studies on (*vide infra*) interesting assemblies for complex **12** justify the role of non-covalent interactions in stabilizing its 2D network structure.

The lattice water molecules are involved in strong O–H···O and C–H···O hydrogen bonding interactions (**Figure 5.16**) with the neighbouring monomeric units. A closer look reveals that each of the lattice water molecules is interacting with three neighbouring molecules. The oxygen atoms of the lattice water molecules (O2, O3) are involved in strong O–H···O hydrogen bonding interactions with the non-coordinated oxygen atoms (O4, O7) of the *2,6-PDC* ligand with distances O3–H3B···O4 = 1.957 Å, O3–H3A···O4 = 2.322 Å and O2–H2B···O7 = 1.966 Å (**Table 5.4**).

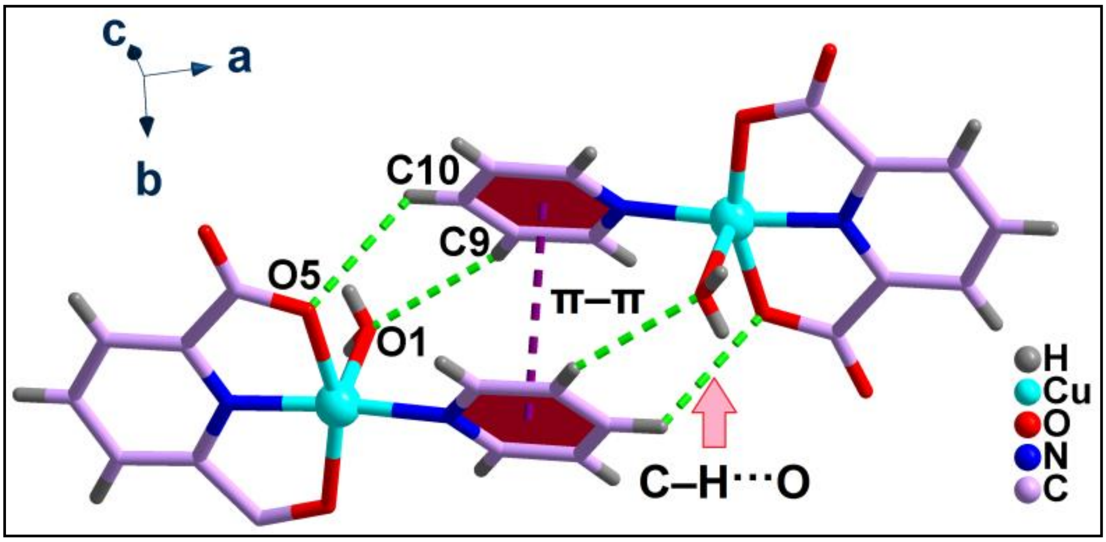

(**a**)

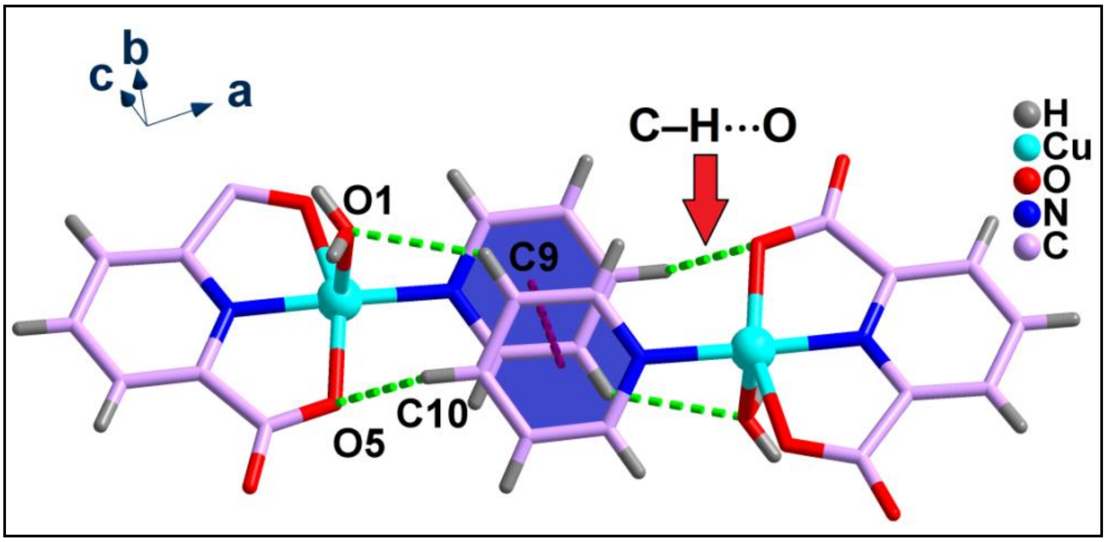

(**b**)

Figure 5.15 Supramolecular dimer formed in the crystal structure of **12**; (**a**) π-stacked dimer; (**b**) on-top representation of the dimer involving C–H···O and π-stacking interactions.

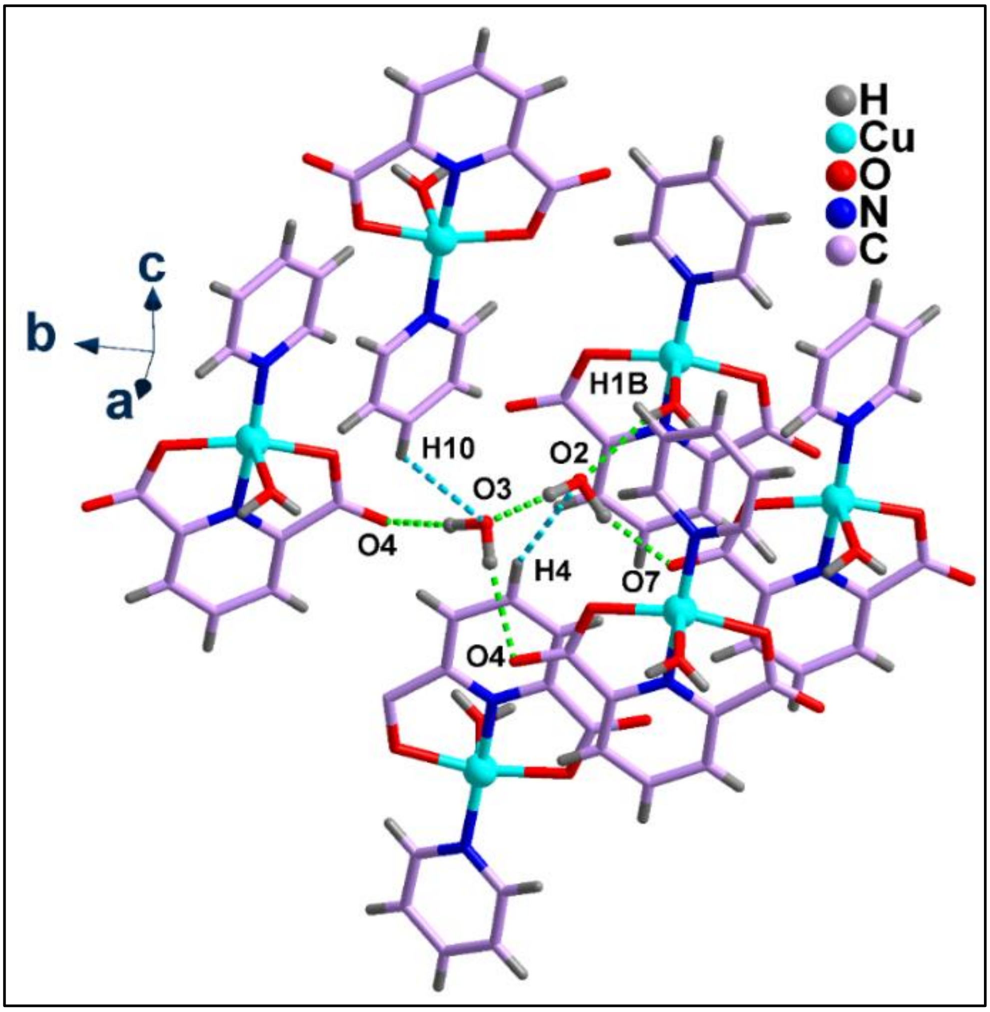

Figure 5.16 O–H···O and C–H···O hydrogen bonding interactions involving lattice water molecules in [Cu(py)(2,6-PDC)(H_2O)]·$2H_2O$ (**12**).

One lattice water molecule (O2) forms O–H···O hydrogen bond with the coordinated aqua ligand with O1–H1B···O2 distance of 2.064 Å. Furthermore, each lattice water molecule is also involved in C–H···O interactions with the –CH moiety of *py* ligand [C4–H4···O2 = 2.697 Å; C10–H10···O3 = 2.996 Å]. The presence of these hydrogen bonding interactions involving the lattice water molecules adds a new dimension to the crystal structure of complex **12**. The 2D adjacent layers of compound **12** get further stacked, like compound **10**, to give rise to an interesting 3D supramolecular framework with 1D channels along the *c*-axis (**Figure 5.17**), enclathrating the lattice water molecules (**Figure 5.18**).

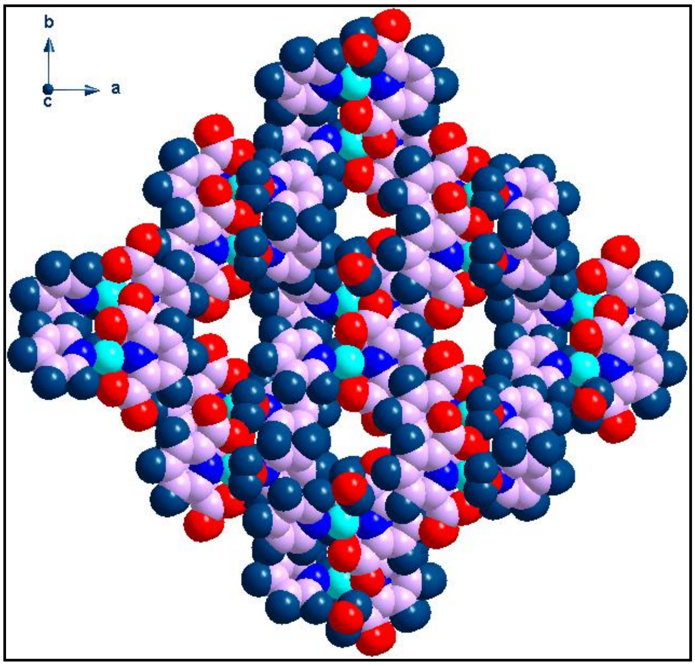

Figure 5.17 A perspective view along the *c*-axis of the 3D network of [Cu(py)(2,6-PDC)(H_2O)]·$2H_2O$ (**12**) showing the 1D open channels.

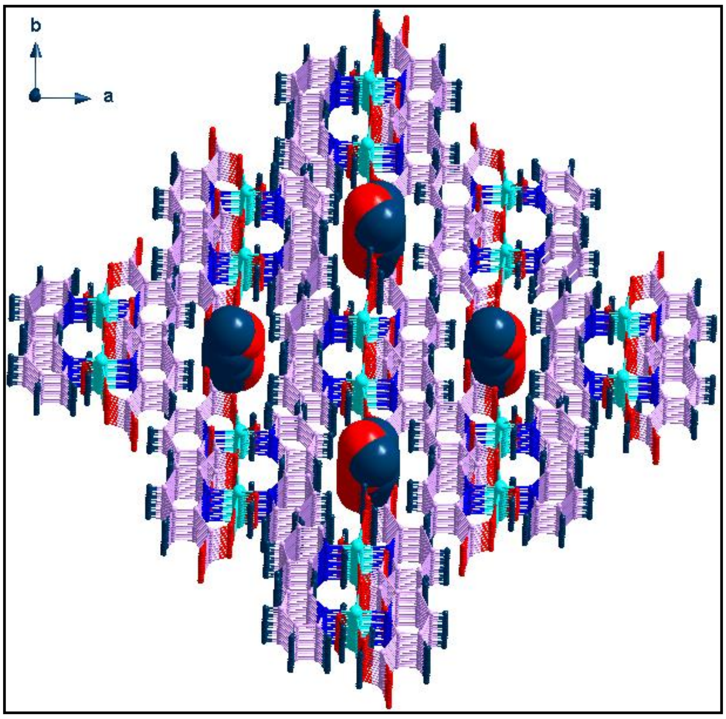

Figure 5.18 A perspective view along the *c*-axis of the 3D network of [Cu(py)(2,6-PDC)(H_2O)]·$2H_2O$ (**12**) showing enclathration of the lattice H_2O molecules (shown in space-filling model) in the 1D channels.

Table 5.4 Selected hydrogen bond distances (Å) and angles (°) for compound **12**.

D–H···A	*d*(D–H)	*d*(D···A)	*d*(H···A)	<(DHA)	Symmetry code
O1–H1A···O6	0.8200	2.8061	1.9967(1)	169.044(3)	x,–y+1/2,+z–1/2
O2–H2B···O3	0.9794	2.8170	1.8482(1)	169.581(3)	x,y,z
O2–H2A···O7	0.9615	2.8867	1.9657(1)	159.661(3)	x,y,z
O3–H3B···O4	0.9512	2.8990	1.9565(1)	170.523(4)	x,+y+1,+z
C3–H3···O7	0.9300	3.4044	2.5622(1)	150.803(5)	–x+1,+y–1/2,–z+1/2
C4–H4···O2	0.9300	3.5695	2.6966(1)	156.666(4)	–x+1,+y–1/2,–z+1/2
C5–H5···O4	0.9300	3.2514	2.4357(1)	146.399(4)	–x+1,+y+1/2,–z+1/2
C8–H8···O2	0.9300	3.5369	2.7519(1)	142.703(3)	x,–y+1/2,+z+1/2
C9–H9···O1	0.9300	3.2571	2.5941(1)	128.671(3)	–x,–y,–z+1
C10–H10···O5	0.9300	3.3422	2.7755(1)	120.268(4)	–x,–y,–z+1
C3–H3···C4	0.9300	3.7099	3.2855(1)	110.138(2)	

5.3.4 Isostructurality of the compounds 10 and 11

The compounds **10** and **11** are structurally identical as they only differ on the basis of the central metal ions present in them and belong to the same structure type and can be termed as isostructural.

The isostructurality of the compounds **10** and **11** has been investigated using Fabian & Kalman approach as discussed in previous chapters. To investigate the isostructurality of the two compounds, we first evaluate some parameters such as unit cell similarity index (Π), mean elongation value ($\in$) and the asphericity index (*A*) as given by;

$\Pi = [(a+b+c)/(a'+b'+c')]-1$, $(a+b+c > a'+b'+c')$, (where, *a*, *b*, *c* and *a*′, *b*′, *c*′ are the orthogonalized lattice parameters of the structures);

$\in = (V'-V)^{1/3}-1$, $V' > V$ (where, *V* and *V*′ are the volumes of the respective unit cells of the two compounds) and

$$A = (2/3)[1-\sum_{j>i}\{[(1+\in)M_i-1]\times[(1+\in)M_j-1]/3\in^2\}]^{1/2}$$

(where, M_i's are the principal axes of matrix M, which gives the pure shear component of the transformation between the two crystallographic coordinate systems).

If the structural similarity between two compounds is very high, then the Π value, $\in$ value and the product $\in A$ (lattice distortion index) are expected to be practically equal to zero.[79] For the compounds **10** and **11**, the values of Π, $\in$ and *A* are found to be 0.00296, 0.00304 and 0.3459 respectively, which supports their structural similarity as obtained from the single crystal XRD analyses. The lattice distortion index *viz.* ∈*A* for the compounds **10** and **11** is found to be 0.00105, which also supports the structural similarity.

The above parameters obtained for the compounds **10** and **11** clearly indicate their structurality of the two crystalline solids. Ambarish and his research group have also reported the unit cell similarity index value of 0.0045 for two isostructural polymeric structures *viz.* $[Cu(L)Cl]_n(ClO_4)_n$ and $[Cu(L)Br]_n(ClO_4)_n$ [where, L = 1,9-diamino-5-methyl-5-nitro-3,7-diazanonane].[80]

5.3.5 Powder X-ray Diffraction

Powder X-ray diffractions of the isostructural compounds **10** and **11** were recorded at room temperature to prove that the synthesized coordination solids of formula $[M(py)(2,6\text{-PDC})(H_2O)_2]\cdot H_2O$ [M = Co(**10**) and Ni(**11**)] are true representatives of their bulk materials. The powder X-ray diffraction pattern of compound **10** (**Figure 5.19**) displays significant deviations from the simulated one. This observation may be due to routine sample preparation (grinding of the compound prior the measurement).[81] It is also possible that phase transformation of compound **10** occurs due to grinding prior to PXRD measurement.[81] The experimental and the simulated powder X-ray diffraction patterns for compound **11** (**Figure 5.20**) are in good agreement with each other, indicating that the compound is true representative of its bulk material. Small differences in reflection intensities and peak positions are observed between the simulated and experimental patterns, which can be attributed to the variation in crystal orientation or particle size of the powder sample.[82]

5.3.6 Theoretical Studies

The theoretical study is devoted to analyze the π–π interactions observed in the solid state structures of the compounds **10**, **11** and **12** focusing our attention to the influence of the *py* coordinated metal centers upon the strength of the interaction. We have first computed the MEP surface of compound **10** as model in order to investigate the most electron rich and electron poor parts of the molecule. The MEP maximum is located at the H-atoms of the coordinated water molecule. The acidity of these H-atoms is enhanced due to the coordination of water to the Co(II) atom. The most negative part is located at the carboxylate groups (–55 kcal/mol). It is interesting to highlight that the

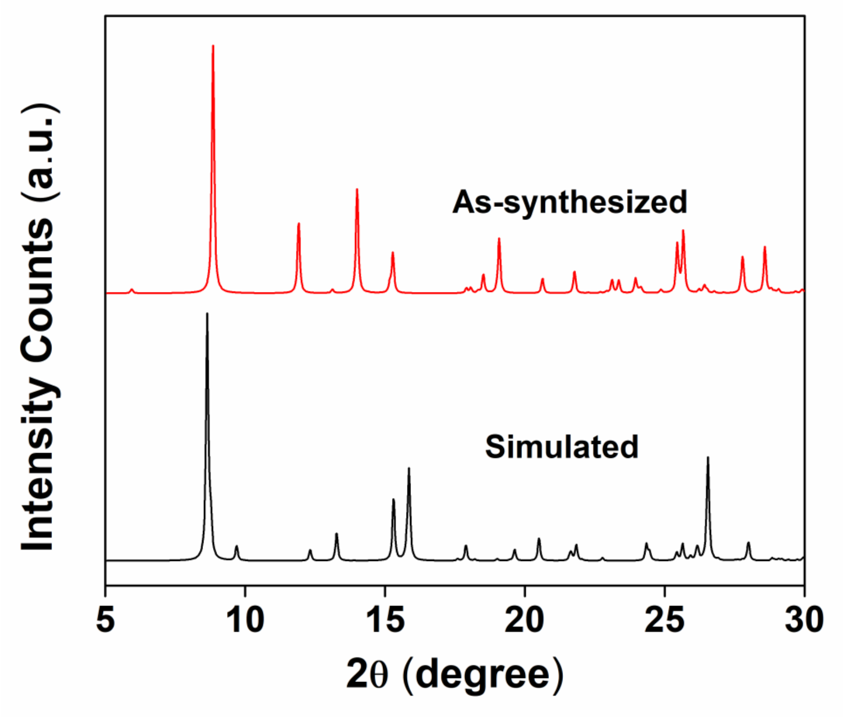

Figure 5.19 Powder X-ray diffraction patterns: as-synthesized (red) and simulated from MERCURY software (black) of [Co(py)(2,6-PDC)(H_2O)$_2$]·H_2O (**10**).

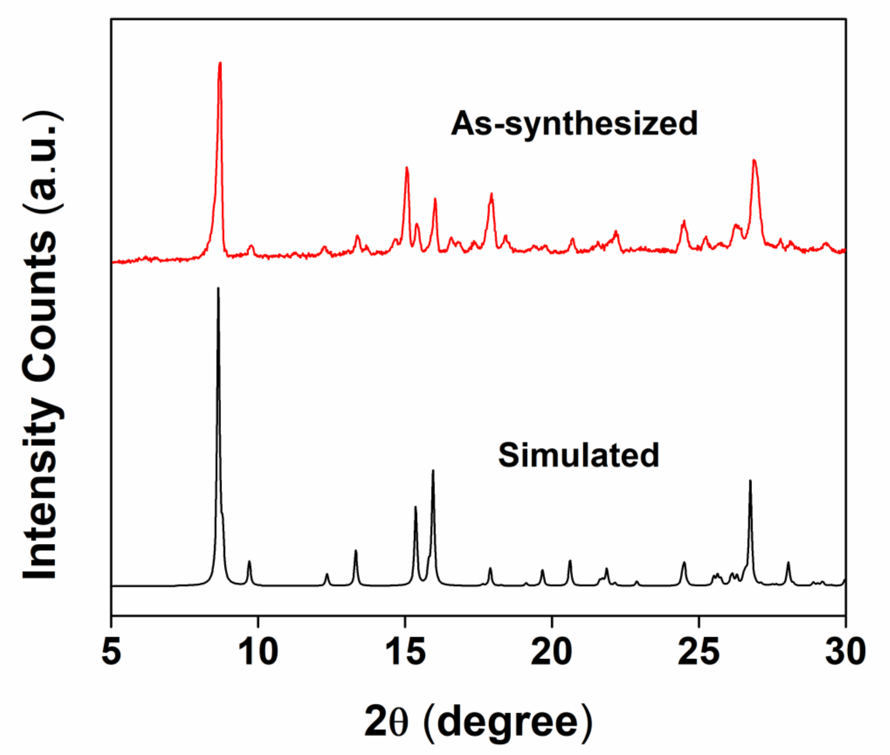

Figure 5.20 Powder X-ray diffraction patterns: as-synthesized (red) and simulated from MERCURY software (black) of [Ni(py)(2,6-PDC)(H_2O)$_2$]·H_2O (**11**).

MEP at the H-atoms of the coordinated *py* are also quite acidic (+30 kcal/mol). Furthermore, the MEP value at the lone pairs of the coordinated water molecule is very small (–6 kcal/mol) (**Figure 5.21**).

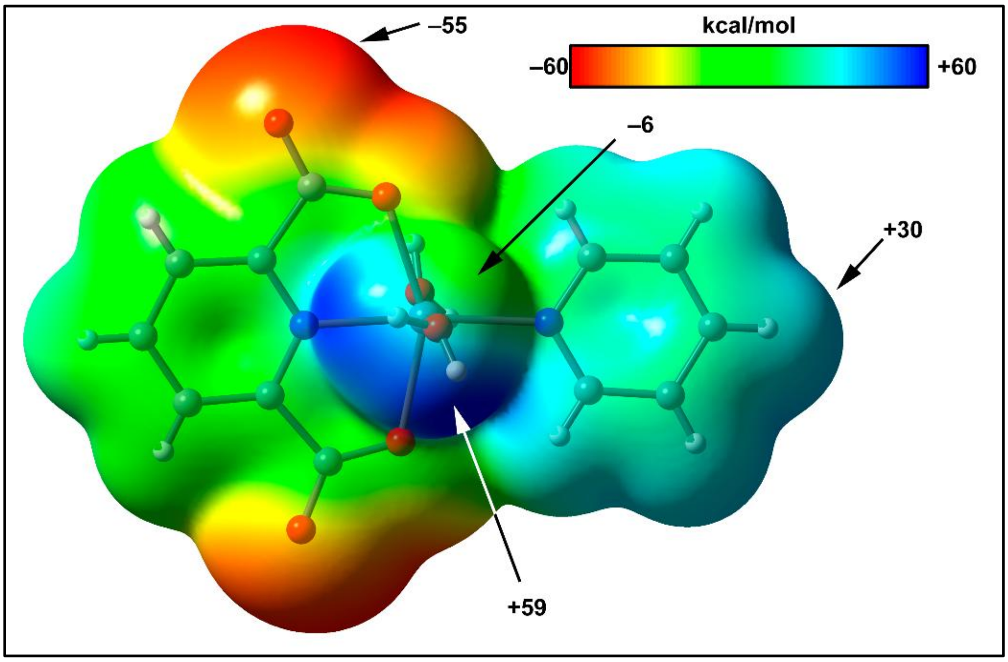

Figure 5.21 Molecular electrostatic potential (MEP) plotted onto the van der Waals surface (isosurface 0.001 a.u.) of compound **10**. The energies at selected points are given in kcal/mol.

We represent the self-assembled dimers that are formed in the X-ray structures of the complexes **10**, **11** and **12** involving *py*. In all cases, the π-stacking is anti-parallel [**Figure 5.22(a)**-(**c**)], and for the Cu atom, the arrangement of the coordinated *py* rings is different compared to isomorphic compounds **10** and **11**. This is clearly appreciated in the on-top representation shown in **Figure 5.22(d)**-(**e**). We have calculated the dimerization energies at the B3LYP-D/def2-TZVP level of theory and they are almost identical for Co (compound **10**) and Ni (compound **11**) metals, $\Delta E_1 = –4.9$ kcal/mol and $\Delta E_2 = –5.0$ kcal/mol, respectively, thus indicating that is a moderately strong interaction. For comparison purposes, we have computed the *py* dimer at the same level and the strength of the interaction is weaker ($\Delta E_{Py\cdots Py}$ = –3.6 kcal/mol) thus indicating a favourable effect of the metal coordination (larger dipole···dipole interaction). The close examination of the dimer shows that one aromatic C–H bond is pointing to the available lone pair of the coordinated water molecule. In order to estimate the π–π stacking interaction without this contribution, we have computed an additional theoretical model where this coordinated water molecule has been eliminated. These mutated complexes are shown in **Figure 5.22(g)-(h)** and the interaction energies are reduced to $\Delta E_4 = -4.2$ kcal/mol and $\Delta E_5 = -4.0$ kcal/mol for Co (**10**) and Ni (**11**), respectively. Consequently, the H-bonds are very weak (< 0.5 kcal/mol each H-bond) in agreement with the small MEP value at the lone pair of the coordinated water molecule. Moreover, the reinforcement of the π-stacking interaction due to the metal coordination of *py* is around 0.5 kcal/mol. Interestingly, the Cu-dimer [**Figure 5.22(c)**] in the complex **12** exhibits a strong interaction energy, $\Delta E_3 = -12.2$ kcal/mol. The π-stacking mode is different and the on-top representation shows that two pairs of symmetrically related C–H···O H-bonds are formed. One pair of H-bonds is similar to that observed in **10** and **11** and involves the coordinated water molecule (2.59 Å).

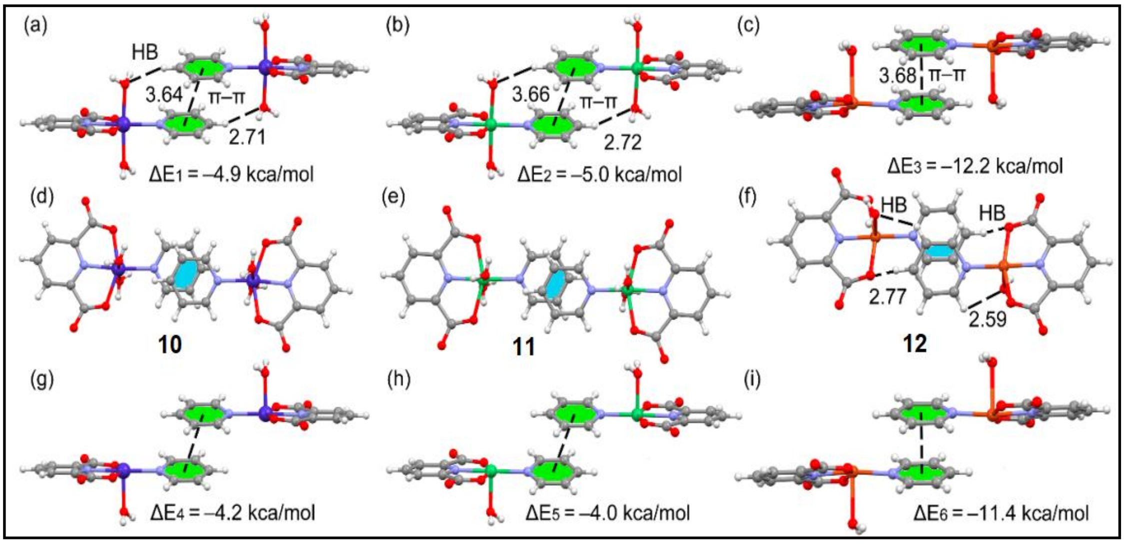

Figure 5.22 Self-assembled π-stacked dimers retrieved from the crystal structures of compounds **10(a)**, **11(b)** and **12(c)**. The on-top representations of the self-assembled dimers are given for compounds **10(d)**, **11(e)** and **12(f)**. The theoretical models used to evaluate the C–H···OH_2 interactions are also indicated for compounds **10(g)**, **11(h)** and **12(i)**. Distances are in Å.

The other pair of H-bonds involves one of the carboxylate groups of *2,6-PDC*. This combination of interactions explains the largest interaction energy observed for this dimer. For this compound we have also computed an additional theoretical model where the coordinated water molecule has been located opposite to the original location [**Figure 5.22(i)**]. As a result, one set of H-bonds are not formed and the interaction energy is slightly reduced to $\Delta E_6 = -11.4$ kcal/mol, thus revealing that the C–H···OH_2 H-bonds are very weak, as observed similarly for the compounds **10** and **11**. The strong nature of the C–H···OOC H-bonds agrees well with the MEP surface analysis commented above, since the value at the carboxylate group is very large and negative.

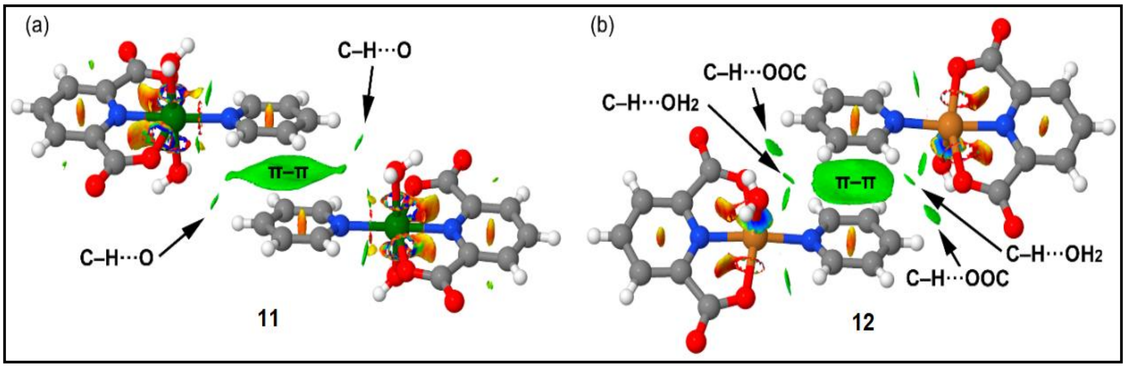

Figure 5.23 NCI surface of the dimers of compounds **11**(**a**) and **12**(**b**). The gradient cut-off is s = 0.35 a.u., and the colour scale is $-0.04 < \rho < 0.04$ a.u.

We have also computed, using the B3LYP-D/def2-TZVP wave function, the "non-covalent interaction plot" (NCI plot) index in order to characterize the anti-parallel π–π interactions in the dimers of compounds **11** (also as model of **10**) and **12**. The NCI plot is an intuitive visualization index that allows the characterization of non-covalent interactions efficiently and, consequently, is convenient to analyze supramolecular interactions since it clearly shows which molecular regions interact. The colour scheme is a red-yellow-green-blue scale with red (repulsive) and blue (attractive). Yellow and green surfaces correspond to weak repulsive and weak attractive interactions, respectively. The representations of the NCI plot for the dimers of compounds **11** and **12** are shown in **Figure 5.23**. For the anti-parallel dimers of compounds **11** and **12**, the π–π interaction is characterized by the presence of a large green isosurface located between the aromatic rings, thus confirming the interaction. In compound **11**, the NCI plot also reveals the existence of a very small isosurface located between the coordinated water O-atom and one CH bond of the aromatic ring [**Figure 5.23**(**a**)]. Such a small and green isosurface agrees well with the energetic analysis summarized in **Figure 5.22** that evidences that the interaction is very weak. For the π-stacked dimer of the complex **12** [**Figure 5.23(b)**], the C–H···OH_2 H-bonds are characterized by small isosurfaces and, on the contrary, the C–H···OOC H-bonds are characterized by larger isosurfaces thus suggesting stronger interaction. This analysis reveals a quite intricate combination of non-covalent bonds influencing the formation of the self-assembled dimer in the complex **12**.

5.3.7 Thermal studies

The thermogravimetric (TG) analyses of the complexes **10**, **11** and **12** were performed in the temperature range from 25 to 700°C under N_2 atmosphere at the heating rate of 10ºC min^{-1}. Almost similar thermal curves were obtained for the complexes **10** and **11** due to their isostructural nature (**Figure 5.24**). The compounds are thermally stable up to 25°C. Above this temperature, the TG curves of the compounds exhibited two main steps of weight loss. The TG curve of **10** showed the first weight loss of 25.67% in the temperature range 58-193°C, corresponding to the loss of two coordinated[83] and one lattice water[84] molecules along with half *py* molecule[85] per formula unit (calculated = 26.22%). Allan and his group also reported such fractional decomposition of *py* molecules in cobalt(II), nickel(II) and copper(II) complexes of 2-(p-tolyl) pyridine.[86a] Momeni *et al.* have also reported similar decomposition of *py* molecules in cobalt(II) coordination compounds of 4′-hydroxy-2,2′,6′,2"-terpyridine.[86b] The second significant weight loss of 54.93% corresponds to the loss of the other half *py* molecule and the *2,6-PDC*[87] in the framework in the temperature range of 186 to 694°C (calculated = 57.61%). The residual weight of 19.05% is attributed to the final product CoO (calculated = 21.10%). The TG plot of complex **11** also showed the weight loss of 34.62% in the first stage between 25-327°C, attributable to the loss of two coordinated and one lattice water molecules along with the *py* molecule per formula unit (calculated = 37.51%). The next weight loss of 45.71% corresponds to the decomposition of *2,6-PDC* in the framework in the temperature range of 327-697°C, (calculated = 46.51%). The remaining weight of 19.67% corresponds to NiO (calculated = 21.04%). For complex **12**, the first stage of the thermal decomposition at 25-261°C is associated with the removal of one coordinated and two lattice water molecules along with the half *py* molecule. The observed weight loss for this step is 27.95% while, calculated is 25.87%. Liptay *et al.* have also observed such fractional decomposition of *py* molecule in transition metal complexes *viz.* $[Ni(py)_4Cl_2]$, $[Mn(py)_4Cl_2]$, $[Mn(py)_2I_2]$.[88] This is followed by another weight loss of 34.53% for complex **12** in the temperature range of 283-697°C that corresponds to the removal of the remaining half of the *py* molecule along with one half of the *2,6-PDC* (calculated = 33.75%).[85]

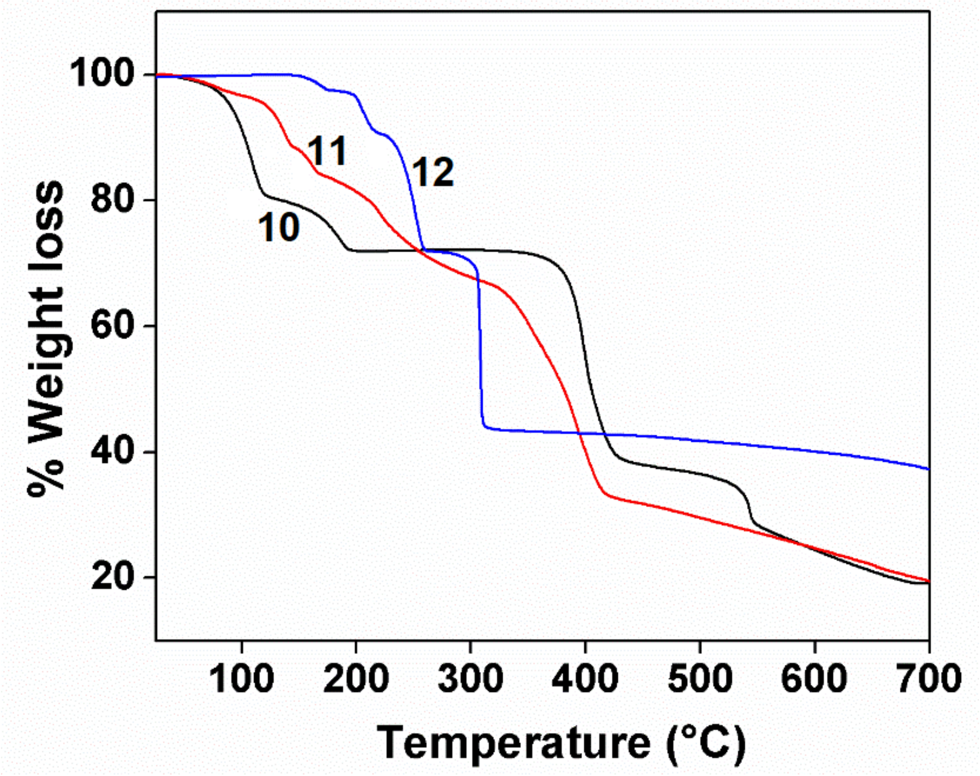

Figure 5.24 Thermogravimetric analysis of the complexes **10**, **11** and **12**.

5.3.8 Cell viability and apoptosis assay

MTT assay is a method used in cell culture to distinguish viable and non-viable cells with regards to quantity in a culture[89] and is a most widely used preliminary screening method for natural products and synthetic compounds for studying cell proliferation and anticancer activities.[90] The complexes **10**, **11** and **12** show significant concentration dependent decrease in cell viability when treated against DL cell lines for 24 hours [**Figure 5.25(b)**]. The cell cytotoxicity (~20-30%) is obtained for the compounds at the dose range from 1-10 μM within 24 hours; with relatively high cytotoxicity for complexes **10** and **12** towards malignant DL cells than normal cells (~10%). This may be due to the fact that as cancer cells undergo rapid abnormal cell proliferation, they are generally more susceptible to these complexes than normal cells. Besides that, cancer cells often have impaired ability to repair DNA damage, which increases the chance that they cannot properly replicate their DNA, eventually causing cell death by mitotic catastrophe or by apoptosis.[91]

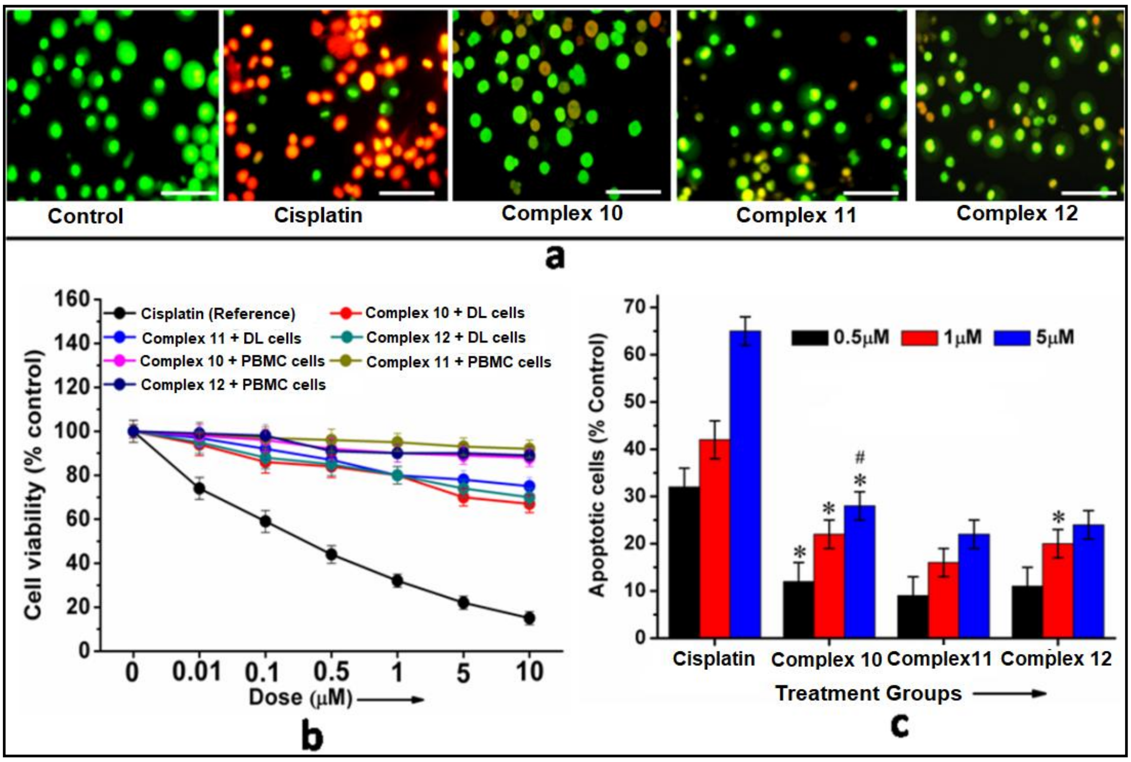

Figure 5.25(**a**) Control DL cells showed mostly viable cells, cisplatin and complexes $[Co(py)(2,6\text{-}PDC)(H_2O)_2]\cdot H_2O$ (**10**), $[Ni(py)(2,6\text{-}PDC)(H_2O)_2]\cdot H_2O$ (**11**) and $[Cu(py)(2,6\text{-}PDC)(H_2O)]\cdot 2H_2O$ (**12**) treated groups showing apoptotic features evident by red/orange nuclei. Scale bar 50 µM. (**b**) cell viability study on DL and PBMC cells after treatment at different dosage (0.01-10 µM) for 24 hours. (**c**) Showed percentage apoptotic cells after treatment with the complexes and the reference drug, cisplatin at different dosage. Data are mean ± S.D., n = 3, ANOVA, $P \leq 0.05$. ANOVA symbol: * with respect to the complex **11** and # with respect to the complex **12**

Apoptosis, as discussed in the previous chapters, is a physiological process of cell death characterized by morphological features and mainly associated with severe DNA damage, the frequency and time of appearance of which depend on the cell line and the apoptosis-inducing signal.[92] Dual staining fluorescent method involving acridine orange and ethidium bromide (AO/EB), visualized under a fluorescent microscope, was used to study the action of the complexes **10**, **11** and **12** in apoptosis-associated changes of cell membranes during the process of apoptosis.[93] Acridine orange (AO) is a vital nucleic acid binding dye that can recognize nuclear DNA across an intact cell membrane by emitting green fluorescence and ethidium bromide (EB) can only detect apoptotic cells by emitting red/orange fluorescence.[94] Apoptotic studies in control group showed mostly viable DL cells that are represented by green fluorescent nuclei [**Figures 5.25(a)** and (**c**)]. Moreover, the concentration-dependent increase in apoptotic features, *viz*. nuclear marginalization, chromatin condensation and fragmentation can be seen for the DL cells treated with the complexes **10**, **11** and **12**. It can be revealed from the results of apoptosis analyses that the reference drug cisplatin can induced more apoptotic cell death against DL cells than that of the complexes.[95] Similar pyridine derivatives have been found to be active as novel apoptosis inducer by triggering DNA damage-mediated p53 phosphorylation (tumor suppressor) in A375 human melanoma cancer cell lines.[96] The anti-proliferative activity along with mitochondria-mediated and caspase-dependent apoptosis of ruthenium pyridyl complexes against cancer cells has also been reported.[97]

5.3.9 Molecular docking studies

The *in silico* docking simulation is an important bioinformatics tool which can be used to develop inhibitors for novel therapeutic targets mostly in the field of medicinal chemistry.[98] *In silico* approach has been utilized recently to study the role of pro- and anti-apoptotic BCL-2 family members in tumourigenesis[99] which allows the development of more efficient and more precisely targeted treatment regimens.[100] In the present chapter, our effort was to establish possible mechanism of action of the synthesized complexes that causes cytotoxicity and apoptosis by analysis the active sites using molecular docking simulation with BCL-2 proteins. Various chemotherapeutic agents inhibit the anti-apoptotic BCL-2 proteins (*used in the present study*) and that are key regulators of apoptosis implicated in human disease including cancer.[101] The docking was validated by redocking the original ligands present in active site of the receptor as observed in crystallographic PDB file (PDB ID: 2O22). Docking studies revealed that the complexes **10**, **11** and **12** have lowest binding energy (high affinity for receptor) and are capable of forming strong hydrogen bonding interactions with the active site amino acids of BCL-2 protein [**Figures 5.26-5.29**]. The *in silico*-docking results reveal that these interactions play an important role for the stability of the target-compound complexes.

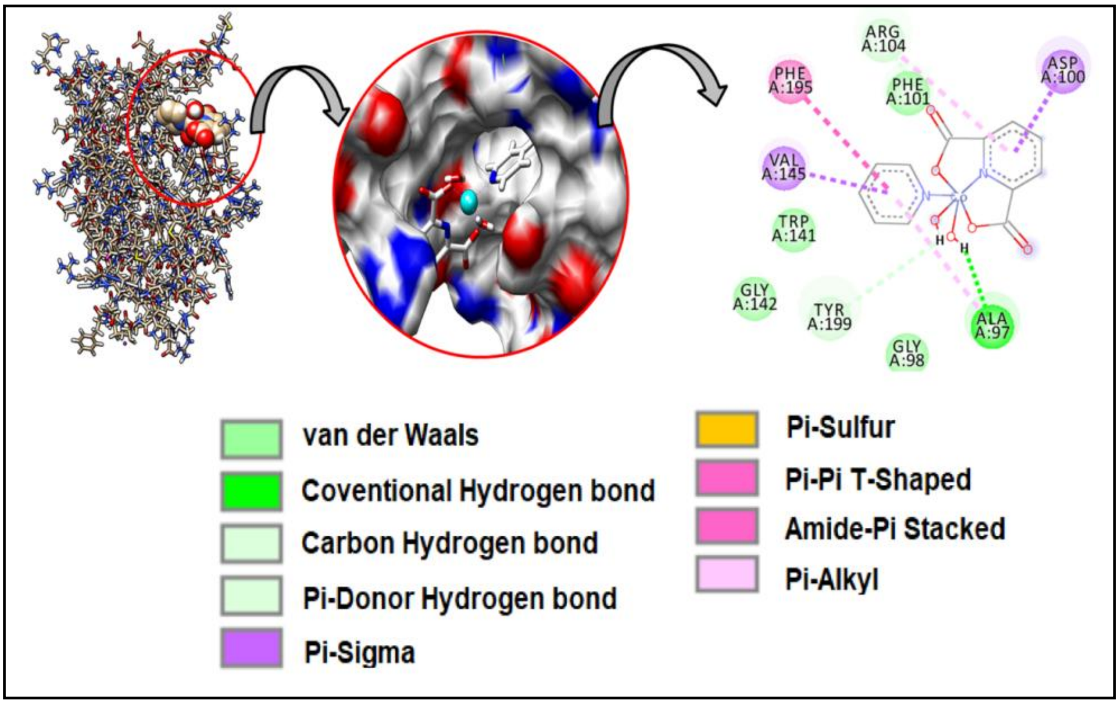

Figure 5.26 Docking structures of the complex [Co(py)(2,6-PDC)$(H_2O)_2$]·H_2O (**10**) with BCL-2 receptor. Chemical interactions are shown in dotted lines along with ligand atoms labeling and interacting amino acids in the active sites of BCL-2 receptor.

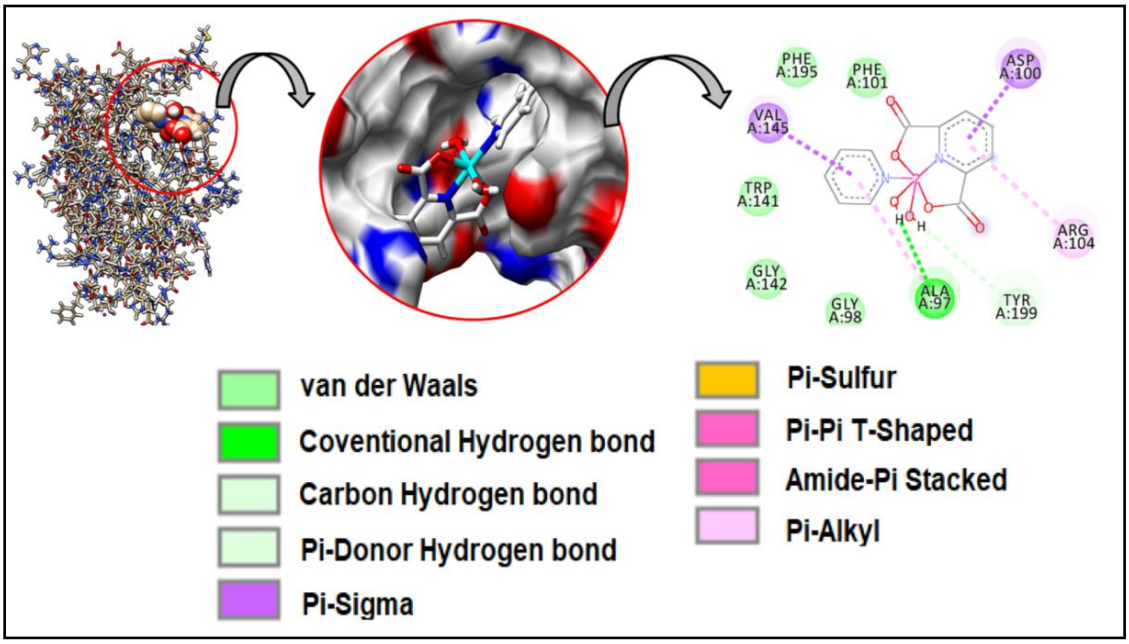

Figure 5.27 Docking structures of the complex [Ni(py)(2,6-PDC)$(H_2O)_2$]·H_2O (**11**) with BCL-2 receptor. Chemical interactions are shown in dotted lines along with ligand atoms labeling and interacting amino acids in the active sites of BCL-2 receptor.

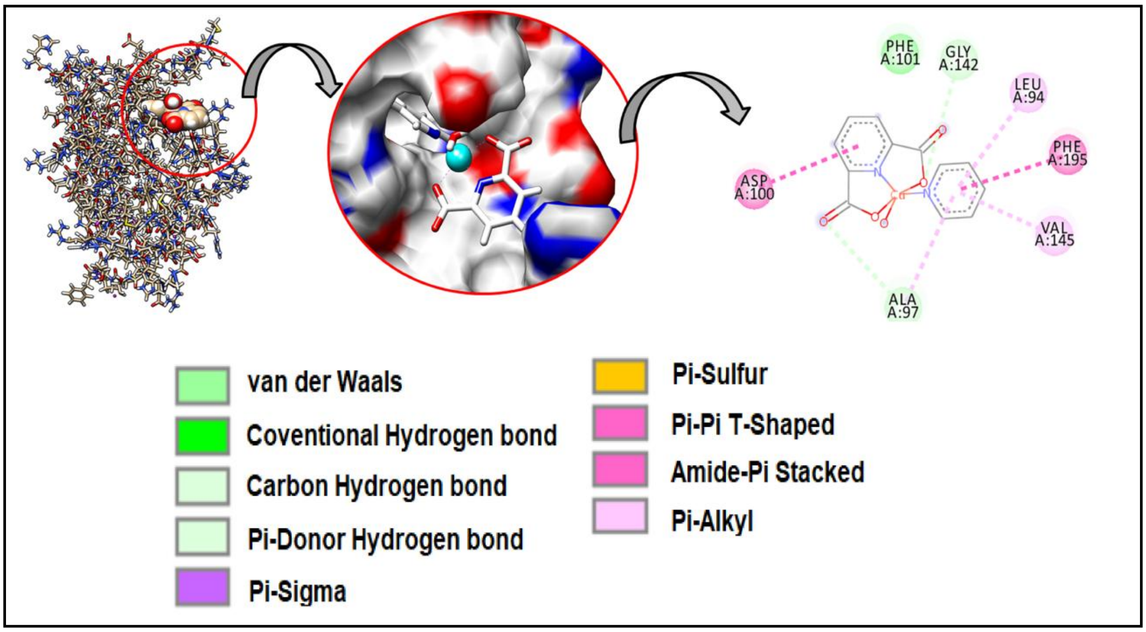

Figure 5.28 Docking structures of the complex [Cu(py)(2,6-PDC)(H_2O)$_2$]·2H_2O (**12**) with BCL-2 receptor. Chemical interactions are shown in dotted lines along with ligand atoms labeling and interacting amino acids in the active sites of BCL-2 receptor.

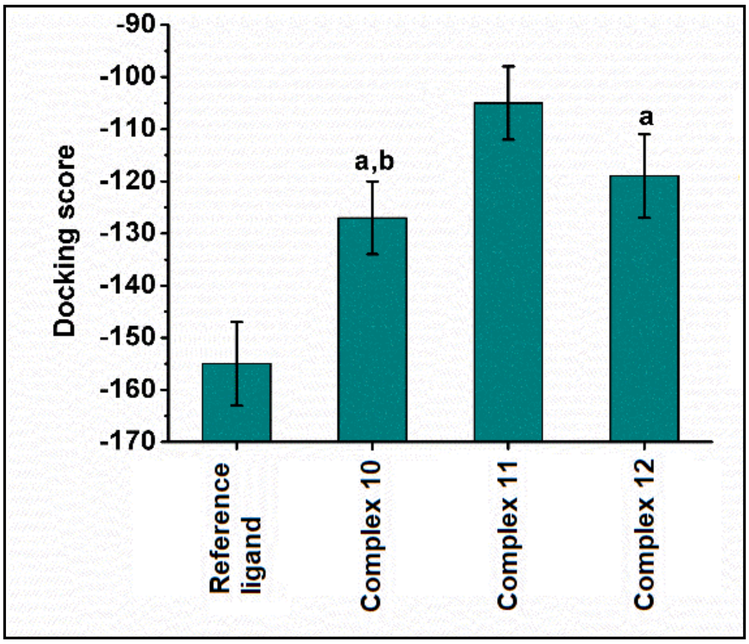

Figure 5.29 Docking scores of complexes [Co(py)(2,6-PDC)(H_2O)$_2$]·H_2O (**10**), [Ni(py)(2,6-PDC)(H_2O)$_2$]·H_2O (**11**) and [Cu(py)(2,6-PDC)(H_2O)$_2$]·2H_2O (**12**) with BCL-2 receptor protein. As per MVD docking score algorithm, lowest the score better is the interactions. Data are mean ± S.D, ANOVA, $P \leq 0.05$. ANOVA significance symbol: **a**, with respect to complex **11** and **b**, with respect to complex **12**.

5.3.10 Pharmacophore modelling

Bioactive compound(s) to be effective as a drug must reach its target destination and stay in the body without losing potency for the expected biological events. In that context, computer models constitute valid alternatives to experiments on animal models. Pharmacophore features involving chemical groups in bioactive compounds are useful signature to identify the essential components of the compounds that show biological activities[102] and are based on structure activity relationship (SAR). Next generation drug discovery process utilizes pharmacophore features to target drugs with more accuracy so that the drugs have very low or no side effects in the host.[103] As discussed in the previous chapters, Ligandscout is a unique software program that highlights key chemical features associated with biological activities[104] along with the 3D-geometries of bioactive molecules. We have identified the important integrated pharmacophore features of the synthesized complexes which include hydrophobic, aromatic, positive ionizable, negative ionizable, H-bond donor and H-bond acceptor that are responsible for biological activities of the complexes (**Figure 5.30**).

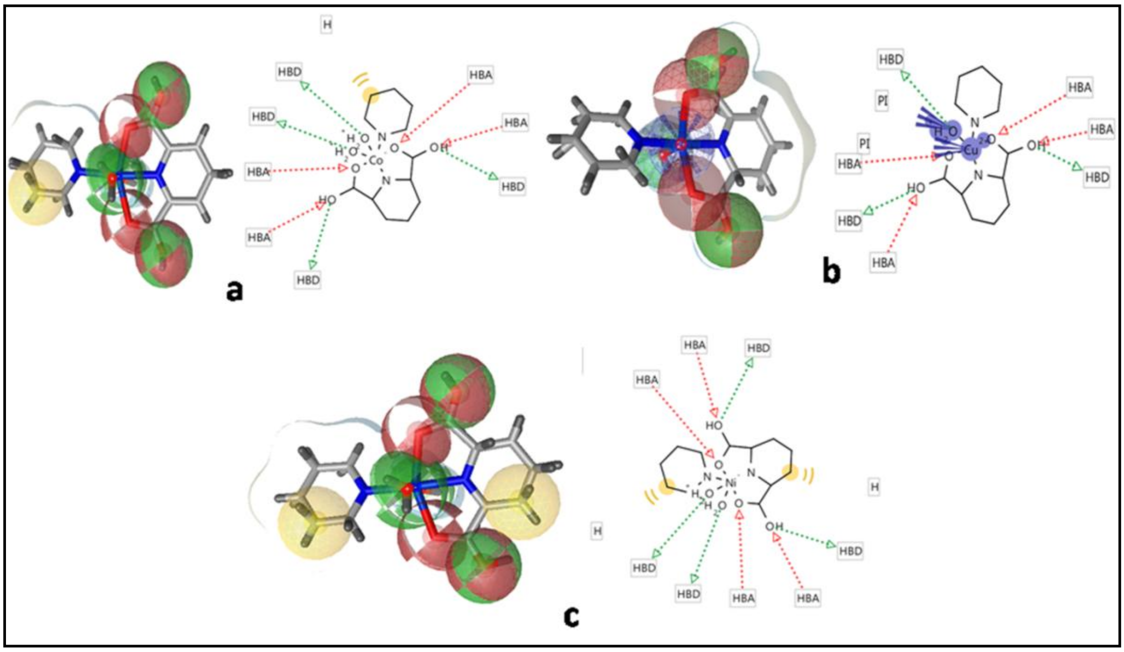

Figure 5.30 Pharmacophore features of the complexes (**a**) [Co(py)(2,6-PDC)$(H_2O)_2$]·H_2O (**10**), (**b**) [Ni(py)(2,6-PDC)$(H_2O)_2$]·H_2O (**11**) and (**c**) [Cu(py)(2,6-PDC)(H_2O)]·$2H_2O$ (**12**) responsible for biological activities. Pharmacophore features that include hydrophobic, positive ionizable, negative ionizable, and acceptor are depicted as yellow spheres, blue star, red star, and red arrows respectively.

5.4 CONCLUSIONS

Three new pyridine based coordination compounds of Co(II), Ni(II) and Cu(II) *viz*. [Co(py)(2,6-PDC)(H_2O)$_2$]·H_2O (**10**), [Ni(py)(2,6-PDC)(H_2O)$_2$]·H_2O (**11**) and [Cu(py)(2,6-PDC)(H_2O)]·2H_2O (**12**) have been synthesized and characterized by single crystal X-ray diffraction, electronic, vibrational spectroscopy and thermogravimetric analysis. The isostructural complexes **10** and **11** are further characterized by PXRD and their isostructurality parameters are evaluated by using Fabian and Kalman approach. Several non-covalent interactions including the antiparallel π-stacking interactions stabilize the layered assemblies in the structures. We have evaluated the strength of the antiparallel π-stacking interactions and the influence of the pyridine coordination to the strength of the stacking assembly using DFT calculations. The dimerization energy of the self-assembled dimer in the layered architecture is larger for complex **12** due to the participation of C–H···O hydrogen bonds involving the carboxylate groups. The antiparallel π-stacking and C–H···O interactions have been characterized by using the NCI plot index, which is in good agreement with the energetic and MEP results. All the three complexes significantly inhibit cell viability by inducing apoptotic cell death in cancer cell line with negligible cytotoxicity in normal cells. Interestingly, the molecular docking study reflects that the complexes **10**, **11** and **12** interact and accommodated well in the active sites of anti-apoptotic protein BCL-2 that might lead to apoptotic cell death. Furthermore, the pharmacophore features embedded with the synthesized complexes may play important role during biological activities.

REFERENCES

1. (a) Siva, V.; Bahadura, S. A.; Shameem, A.; Murugana, A.; Athimoolam, S.; Suresh, M. *Opt. Mater.* **2019**, *96*, 109290.

(b) Islam, S.; Datta, J.; Maity, S.; Dutta, B.; Ahmed, F.; Ghosh, P.; Ray, P. P.; Mir, M. H. *ChemistrySelect* **2019**, *4*, 3294.

(c) Aguilà, D.; Jeannin, O.; Jeon, M. F. *Inorg. Chem.* **2018**, *57*, 7892.

(d) Wang, X.; Yao, W.; Qi, Y. F.; Luo, M. F.; Wang, Y. H.; Xie, H. W.; Yu, Y.; Ma, R. Y.; Li, Y. G. *CrystEngComm*. **2011**, *13*, 2542.

(e) Zhang, D.; Martinez, A.; Dutasta, J. *Chem. Rev*. **2017**, *117*, 4900.

2. (a) Maspoch, D.; Ruiz-Molina, D.; Veciana, J. *Chem. Soc. Rev*. **2007**, *36*, 770.

(b) Robin, A. Y.; Fromm, K. M. *Coord. Chem. Rev*. **2006**, *250*, 2127.

(c) Carlucci, L.; Ciani, G.; Proserpio, D. M. *Coord. Chem. Rev*. **2003**, *246*, 247.

3. (a) Adam, R.; Mon, M.; Greco, R.; Kalinke, L. H. G.; Vidal-Moya, A.; Fernandez, A.; Winpenny, R. E. P.; Doménech-Carbó, A.; Leyva-Pérez, A.; Armentano, D.; Pardo, E.; Ferrando-Soria, J. *J. Am. Chem. Soc.* **2019**, *141*, 10350.

(b) Bhattacharyya, M. K.; Saha, U.; Dutta, D.; Frontera, A.; Verma, A. K.; Sharma, P.; Das, A. *New J. Chem*. **2020**, *44*, 4504.

(c) Aakeroy, C. B.; Champness, N. R.; Janiak, C. *CrystEngComm.* **2010**, *12*, 22.

4. (a) Casini, A.; Woods, B.; Wenzel, M. *Inorg. Chem*. **2017**, *56*, 14715.

(b) Schneider, H. J. *Angew. Chem. Int. Ed*. **2009**, *48*, 3924.

5. Yuan, G. Y.; Zhang, L.; Wang, M. J.; Zhang, K. L. *Acta Cryst*. **2016**, *72*, 939.

(b) Eshtiagh-Hosseini, H.; Mirzaei, M.; Biabani, M.; Lippolis, V.; Chahkandi, M.; Bazzicalupi, C. *CrystEngComm.* **2013**, *15*, 6752.

(c) Nath, H.; Dutta, D.; Sharma, P.; Frontera, A.; Verma, A. K.; Barceló-Oliver, M.; Devi, M.; Bhattacharyya, M. K. *Dalton Trans*. **2020**, *49*, 9863.

6. (a) Wang, Y.; Zhou, Y.; Hao, H.; Song, M.; Zhang, N.; Yao, S.; Yan, J.; Zhang, Z.; Lu, T. *Inorg. Chem.* **2018**, *57*, 1342.

(b) Chang, H.; Hou, S.; Cui, G.; Wang, S. *J. Inorg. Organomet. Polym. Mater.* **2017**, *27*, 518.

(c) Georges, M.; Nans, R.; Inhar, I.; Carine, D.; Jean-Pascal, S. *Cryst. Growth Des.* **2010**, *10*, 4906.

(d) Pierre, D.; Sylvie, F.; Nathalie, K.; Wais, H. M. *Chem. Commun.* **2010**, *46,* 868.

(e) Krichen, F.; Walha, S.; Lhoste, J.; Bulou, A.; Kabadou, A.; Goutenoire, F. *J. Mol. Struct*. **2017**, *1146*, 409.

7. Meggers, E. *Chem. Comm*. **2009**, *9*, 1001.

8. (a) Ma, J. F.; Liu, J. F.; Xing, Y.; Jia, H. Q.; Lin, Y. H. *Dalton Trans*. **2000**, 2403.

(b) Aakeröy, C. B.; Champness, N. R.; Janiak, C. *CrystEngComm*. **2010**, *12*, 22.

9. (a) Khavasi, H. R.; Sadegh, B. M. M. *Inorg. Chem*. **2010**, *49,* 5356.

(b) Jung, O. S.; Park, S. H.; Kim, K. M.; Jang, H. G. *Inorg. Chem*. **1998**, *37*, 5781.

10. (a) Noro, S.; Kitagawa, S.; Nakamura, T.; Wada, T. *Inorg. Chem*. **2005**, *44*, 3960.

(b) Munakata, M.; Kitagawa, S. *Inorg. Chim. Acta* **1990**, *169*, 225.

11. (a) Aakeröy, C. B.; Champness, N. R.; Janiak, C. *CrystEngComm.* **2010**, *12*, 22.

(b) Ye, B. H.; Tong, M. L.; Chen, X. M. *Coord. Chem. Rev*. **2005**, *249*, 545.

12. (a) Ovejero, P.; Mayoral, M. J.; Cano, M.; Campo, J. A.; Heras, J. V.; Pinilla, E.; Torres, M. R. J. *Organomet. Chem*. **2007**, *692*, 4093.

(b) (a) Ye, B. H.; Tong, M. L.; Chen, X. M. *Coord. Chem. Rev*. **2005**, *249*, 545.

13. (a) Devereux, M.; McCann, M.; Leon, V.; McKee, V.; Ball, R. J. *Polyhedron* **2002**, *21*, 1063.

(b) Ma, C. B.; Chen, C. N.; Liu, Q. T.; Liao, D. Z.; Li, L. C. *Eur. J. Inorg. Chem*. **2003**, 1227.

14. (a) Wang, Z.; Valtchev, V.; Fang, Q.; Li, X.; Pan, Y. *Inorg. Nano-met. Chem.* **2019**, *49*, 1.

(b) Li, J. H.; Zhu, M. D.; Huang, Q. Y. *Acta Cryst*. **2017**, *73*, 91.

(c) Lian, X. M.; Zhao, W.; Zhao, X. L. *J. Solid State Chem*. **2013**, *200*, 265.

(d) Bauer, W.; Lochenie, C.; Weber, B. *Dalton Trans*. **2014**, *43*, 1990.

(e) Zahedi, M.; Shaabani, B.; Englert, U.; Rad-yousefnia, N; Blake, G. R.; Kazak, C. *Polyhedron* **2017**, *113*, 110.

15. (a) Chuasaard, T.; Panyarat, K.; Rodlamul, P.; Chainok, K.; Yimklan, S.; Rujiwatra, A. *Cryst. Growth Des*. **2017**, *17*, 1045.

(b) Gangu, K. K.; Mukkamala, S. B. *Synth. React. Inorg. Met. Org. Nano-Metal Chem.* **2016**, *46*, 98.

(c) Wan, L.; Zhang, C.; Xing, Y.; Li, Z.; Xing, N.; Wan, L.; Shan, H. *Inorg. Chem*. **2012**, *51*, 6517.

(d) Zhou, S.; Xue, X.; Wang, J.; Dong, Y.; Jiang, B.; Wei, D.; Wana, M.; Jia, Y. *J. Mater. Chem.* **2012**, *22*, 22774.

16. (a) Vasquez-Ríos, M. G.; Rojas-León, I.; Montes-Tolentino, P.; Fernando, I.; Ahuactzi, H.; Höpfl, H. *Cryst. Growth Des*. **2018**, *18*, 7132.

(b) Liu, Y. L.; Kravtsov, V. C.; Beauchamp, D. A.; Eubank, J. F.; Eddaoudi, M. *J. Am. Chem. Soc*. **2005**, *127*, 7266.

(c) Wei, Y. L.; Hou, H. W.; Li, L. K.; Fan, Y. T.; Zhou, Y. *Cryst. Growth Des*. **2005**, *15*, 1405.

17. (a) Li, W.; Chen, S.; Han, S.; Zhao, Y. *J. Solid State Chem*. **2020**, *283*, 121133.

(b) Liu, Z.; Zhao, Y.; Zhang, X.; Kang, Y.; Lu, Q.; Azam, M.; Al-Resayes, S.; Sun, W. *Dalton Trans*. **2017**, *46*, 13943.

(c) Lin, Y.; Zhang, X.; Chen, W.; Shi, W.; Cheng, P. *Inorg. Chem.* **2017**, *56*, 11768.

18. Tella, A. C.; Obaleye, J. A.; Olawale, M. D.; Ngororabang, J. M. V.; Ogunlaja, A. S.; Bourne, S. A. *Comptes. Rendus. Chimie*. **2019**, *22*, 3.

19. Moschovitis, K.; Banti, C. N.; Kourkoumelis, N.; Moushi, E.; Lazaridis, T.; Hadjikakou, S. K. *Inorg. Chim. Acta* **2020**, *500*, 119209.

20. Garin, A. B.; Rakaric, D.; Andric, E. K.; Kosanovic, M. M.; Balic, T.; Perdih, F. *Polyhedron* **2019**, *166*, 226.

21. (a) Wang, Y.; Li, C. *Inorg. Chem. Comm*. **2018**, *96*, 180.

(b) Yang, Y.; Ju, Y.; Jiang, H.; Sun, X; Wu, S.; Zhang, Z. *Inorg. Nano-Met. Chem.* **2017**, *47*, 703.

(c) Lin, S.; Liu, X.; Tan, L.; Cui, Z.; Yang, X.; Yeung, K. W. K.; Pan, H.; Wu, S. *Appl. Mater. Interfaces* **2017**, *9*, 19248.

22. (a) Xiao, H.; Li, X.; Qin, G.; Xia, Y.; Zhou, G. *J. Iran. Chem. Soc*. **2016**, *13*, 793.

(b) Sadjadi, S.; Akbari, M.; Kahangi, F. G.; Heravi, M. M. *Polyhedron* **2020**, *179*, 114375.

23. (a) Siddiqi, Z. A.; Shahid, M.; Kumar, S.; Khalid, M.; Noor, S. J. *Organomet. Chem*. **2009**, *694*, 3768.

(b) Gabr, I. M.; El-Asmy, H. A.; Emmam, M. S.; Mostafa, S. I. *Transit. Met. Chem*. **2009**, *34*, 409.

24. García-Valdivia, A. A.; Cepeda, J.; Fernández, B.; Odonnell, M. M.; Oyarzabal, I.; Parra, J.; Jannus, F.; Choquesillo-Lazarte, D.; García, J. A.; Lupiáñez, J. A.; Gómez-Ruiz, S.; Reyes-Zurita , F.; Rodríguez-Diéguez, A. *J. Inorg. Biochem*. **2020**, *207*, 111051.

25. Bordbar, M.; Tabatabaee, M.; Alizadeh-Nouqi, M.; Mehri-Lighvan, Z.; Khavasi, H. R.; Yeganeh, A.; Fallahian, F.; Dolati, M. *J. Iran. Chem. Soc*. **2016**, *13*, 1125.

26. Wang, X.; Liu, X.; Tian, L. *Main Group Met. Chem*. **2014**, *37*, 143.

27. Said, M. I.; El-Said, A. I.; Aly, A. A. M.; Abou-Taleb, A. *Ultrason. Sonochem*. **2018**, *46*, 68.

28. (a) Mandal, T.; Dey, A.; Seth, S. K.; Ortega-Castro, J.; Rheingold, A. L.; Ray, P. P.; Frontera, A.; Mukhopadhyay, S. *ACS Omega* **2020**, *5*, 460.

(b) Barman, N.; Banerjee, S.; Brandão, P.; Bauzá, A.; Frontera, A.; Saha, A. *J. Coord. Chem*. **2016**, *69*, 1188.

(c) Neel, A. J.; Hilton, M. J.; Sigman, M. S.; Toste, F. D. *Nature* **2017**, *543*, 637.

29. (a) Dawoud, A.; Yaseen, B.; *J. Mol. Liq*. **2017**, *227*, 280.

(b) Quiñone, D.; Martínez, S.; Bozoglián, F.; Bazzicalupi, C.; Torres, J.; Veiga, N.; Bianchi, A.; Kremer, C. *ChemPlusChem*. **2019**, *84*, 540.

30. (a) Liu, K.; Shan, Q.; Nie, J.; Yan, X. *Z. Anorg. Allg. Chem*. **2018**, *644*, 82.

(b) Mamada, M.; Minami, T.; Katagiri, H.; Omiyaa, T.; Tokitoa, S. *Chem. Comm*. **2017**, *53*, 8834.

31. Wheeler, S. E.; Houk, K. N. *J. Am. Chem. Soc*. **2008**, *130*, 10854.

32. Sikorski, A.; Trzybiński, D. *J. Mol. Struct*. **2013**, *1049*, 90.

33. (a) Kang, J.; Tangadanchu, V. K. R.; Gopala, L.; Gao, W.; Cheng, Y.; Liu, H.; Geng, R.; Li, S.; Zhou, C. *Chin. Chem. Lett*. **2017**, *28*, 1369.

(b) Bhattacharyya, M. K.; Saha, U.; Dutta, D.; Das, A.; Verma, A. K.; Frontera, A. *RSC Adv*. **2019**, *9*, 16339.

34. Qin, X.; Liu, Y.; Yu, Q.; Yang, L.; Liu, Y.; Zhou, Y.; Liu, J. *Chem. Med. Chem*. **2014**, *9*, 1665.

35. Sikdar, Y.; Modak, R.; Bose, D.; Banerjee, S.; Bieńko, D.; Zierkiewicz, W.; Bieńko, A.; Saha, K. D.; Goswami, S. *Dalton Trans*. **2015**, *44*, 8876.

36. SADABS, V2.05, Bruker AXS, Madison, USA, **1999**

37. Sheldrick, G. M. *Acta Crystallogr. Sect. A: Found. Crystallogr.* **2008**, *64*, 112.

38. Brandenburg, K. *Diamond 3.1f, Crystal Impact GbR*, Bonn, Germany, **2008**

39. Frisch, M. J.; Trucks, G. W.; Schlegel, H. B.; Scuseria, G. E.; Robb, M. A.; Cheeseman, J. R.; Scalmani, G.; Barone, V.; Mennucci, B.; Petersson, G. A.; Nakatsuji, H.; Caricato, M.; Li, X.; Hratchian, H. P.; Izmaylov, A. F.; Bloino, J.; Zheng, G.; Sonnenberg, J. L.; Hada, M.; Ehara, M. Toyota, K.; Fukuda, R.; Hasegawa, J.; Ishida, M.; Nakajima, T.; Honda, Y.; Kitao, O.; Nakai, H.; Vreven, T.; Montgomery Jr., J. A.; Peralta, J. E.; Ogliaro, F.; Bearpark, M.; Heyd, J. J.; Brothers, E.; Kudin, K. N.; Staroverov, V. N.; Kobayashi, R.; Normand, J.; Raghavachari, K.; Rendell, A.; Burant, J. C.; Iyengar, S. S.; Tomasi, J.; Cossi, M.; Rega, N.; Millam, J. M.; Klene, M.; Knox, J. E.; Cross, J. B.; Bakken, V.; Adamo, C.; Jaramillo, J.; Gomperts, R.; Stratmann, R. E.; Yazyev, O.; Austin, A. J.; Cammi, R.; Pomelli, C.; Ochterski, J. W.; Martin, R. L.; Morokuma, K.; Zakrzewski, V. G.; Voth, G. A.; Salvador, P.; Dannenberg, J. J.;

Dapprich, S.; Daniels, A. D.; Farkas, Ö.; Foresman, J. B.; Ortiz, J. V.; Cioslowski, J.; Fox, D. J. *Gaussian 09, Gaussian Inc.,* Wallingford C. T. **2009**.

40. Grimme, S.; Antony, J.; Ehrlich, S.; Krieg, H. *J. Chem. Phys.* **2010**, *132*, 154

41. Boys, S. F.; Bernardi, F. *Mol. Phys.* **1970**, *19*, 553.

42. Contreras-García, J.; Johnson, E. R.; Keinan, S.; Chaudret, R.; Piquemal, J. P.; Beratan, D. N.; Yang, W. *J. Chem. Theory Comput*. **2011**, *7*, 625.

43. (a) Mosmann, T. *J. Immunol. Methods* **1983**, *65*, 55.

(b) Verma, A. K.; Prasad, S. B. *Anticancer Agents Med. Chem*. **2013**, *13*, 1096.

44. Squier, M. K. T.; Cohen, J. J. *Mol. Biotechnol*. **2001**, *19*, 305.

45. Prasad, S. B.; Verma, A. K. *Microsc. Microanal*. **2013**, *19*, 1377.

46. Vucicevic, J.; Nikolic, K.; Mitchell, J. B. O. *Curr. Med. Chem.* **2019**, *26*, 3874.

47. Salam, A. A. A.; Nayek, U.; Sunil, D. *Curr. Top. Med. Chem.* **2018**, *18*, 2633.

48. Yip, K. W.; Reed J. C. *Oncogene* **2008**, *27*, 6398.

49. Rahman, Y.; Afrin, S.; Tabish, M. *Arch. Biochem. Biophys*. **2018**, *652*, 27.

50. Gabra, M. T.; El-Gohary, N. S.; El-Bendary, E. R.; El-Kerdawy, M. M.; Ni, N. *Eur. J. Med. Chem.* **2017**, *128*, 36.

51. (a) Martak, F.; Cahyani, N. W. D.; Nugraheni, Z. V.; Utomo, W. P. *Indones. J. Chem.* **2016**, *16*, 260;

(b) Roy, S.; Sarkar, S. K.; Saha, R.; Mondal, T. K.; Sinha, C. *Inorg. Chim. Acta* **2018**, *482*, 659.

52. (a) Bellamy, L. J. The Infrared Spectra of Complex Molecules, second ed., vol. 2, Chapman & Hall, London/New York, **1980**.

(b) Nakamoto, K. Infrared and Raman Spectra of Inorganic and Coordination Compounds, fifth ed., John Wiley & Sons, New York, **1997**.

53. Orhan, O.; Çolak, A. T.; Emen, F. M.; Kismali, G.; Meral, O.; Sel, T.; Çilgi, G. K.; Taş, M. *J. Coord. Chem.* **2015**, *68*, 4003.

54. Ay, B.; Yildiz, E.; Kani, İ. *J. Solid State Chem.* **2016**, *233*, 44.

55. Tamer, Ö.; Tamer, S. A.; İdil, Ö.; Avc, D.; Vural, H.; Atalay, Y. *J. Mol. Struct.* **2018**, *1152*, 399.

56. (a) Yang, L.; Liu, L.; Wu, L.; Zhang, H.; Song, S. *Dyes Pigments* **2014**, *105*, 180.

(b) Łyszczek, R.; Mazur, L. *Polyhedron* **2012**, *41*, 7.

57. Ay, B.; Yildiz, E.; Kani, I. *Polyhedron* **2018**, *142*, 1.

58. Wan, L.; Zhang, C.; Xing, Y.; Li, Z.; Xing, N.; Wan, L.; Shan, H. *Inorg. Chem.* **2012**, *51*, 6517.

59. Shams, H.; Derikvand, Z.; Dusek, M.; Eigner, V.; Shokrollahi, A.; Refahi, M.; Azadbakht, A. *J. Iran. Chem. Soc.* **2017**, *14*, 811.

60. Gill, N. S.; Nuttall, R. H.; Scaife, D. E.; Sharp, D. W. A. *J. lnorg. Nucl. Chem.* **1961**, *18*, 79.

61. Basumatary, D.; Lal, R. A.; Kumar, A. *J. Mol. Struct*. **2015**, *1092*, 122.

62. Bora, S. J.; Das, B. K. *J. Solid State Chem*. **2012**, *192*, 93.

63. Akinyele, O. F.; Akinnusi, T. O.; Ajayeoba, T. A.; Ayeni, A. O.; Durosinmi, L. M. *Sci. J. Chem.* **2019**, *7*, 67.

64. Mautner, F. A.; Scherzer, M.; Berger, C.; Fischer, R. C.; Vicente, R.; Massoud, S. S. *Polyhedron* **2015**, *85*, 20.

65. Figgis, B. N.; Hitchman, M. A. Ligand Field Theory and Its Applications, 209, Wiley-VCH, New York, **2000**.

66. Crisóstomo-Lucas, C.; Navarro-Peñaloza, R.; Ortiz-Pastrana, N.; Sánchez-Bartéz, F.; Gracia-Mora, I.; Barba-Behrens, N. *J. Mex. Chem. Soc*. **2018**, *62*, 225.

67. Tandon, S. S.; Chen, L.; Thompson, L. K.; Bridson, J. N. *Inorg. Chem*. **1994**, *33*, 490.

68. (a) Kumar, S.; Sharma, R. P.; Venugopalan, P.; Aree, T.; Ferretti, V. *J. Mol. Struct*. **2015**, *1092*, 225.

(b) Sharma, R. P.; Saini, A.; Singh, S.; Venugopalan, P.; Harrison, W. T. A. *J. Fluorine Chem*. **2010**, *131*, 456.

69. Dutta, D.; Islam, S. M. N.; Saha, U.; Frontera, A.; Bhattacharyya, M. K. *J. Mol. Struct*. **2019**, *1195*, 733.

70. Ghosh, M.; Majee, A.; Nethaji, M.; Chattopadhyay, T. *Inorg. Chim. Acta* **2009**, *362*, 2052.

71. Egli, M.; Sarkhel, S. *Acc. Chem. Res*. **2007**, *40*, 197.

72. Manna, P.; Seth, S. K.; Das, A.; Hemming, J.; Prendergast, R.; Helliwell, M.; Choudhury, S. R.; Frontera, A.; Mukhopadhyay, S. *Inorg. Chem*. **2012**, *51*, 3557.

73. Biswas, C.; Drew, M. G. B.; Escudero, D.; Frontera, A.; Ghosh, A. *Eur. J. Inorg. Chem*. **2009**, *2238*.

74. Etter, M. C. *Acc. Chem. Res*. **1990**, *23*, 120.

75. Batsanov, A. S.; Davidson, M. G.; Howard, J. A. K.; Lamb, S.; Lustig, C. *Chem. Comm*. **1996**, *1791*.

76. Bazargan, M.; Mirzaei, M.; Eshtiagh-Hosseini, H.; Mague, J. T.; Bauzá, A.; Frontera, A. *Inorg. Chim. Acta* **2016**, *449*, 44.

77. (a) Addison, A. W.; Rao, T.; Reedijk, J.; Rijn, J. V.; Verschoor, G. *Dalton Trans*. **1984**, *1349*.

(b) Sancheti, R. S.; Bendre, R. S.; Kumbhar, A. A. *Polyhedron* **2012**, *31*, 12.

78. Dehghanpour, S.; Asadizadeh, S.; Assou, J. *Z. Anorg. Allg. Chem*. **2012**, *638(5)*, 861.

79. Fábián, L.; Kálmán, A., *Acta Cryst*. **1999**, *B55*, 1099.

80. Ray, A.; Maiti, D.; Sheldrick, W. S.; Mayer-Figge, H.; Mondal, S.; Mukherjee, M.; Gao, S.; Ali, M. *Inorg. Chim. Acta* **2005**, *358*, 3471.

81. Balić, T.; Popović, Z.; Marković, B. *Inorg. Chim. Acta* **2018**, *478*, 32.

82. Borah, S.; Kalita, A. C.; Gogoi, N. *Z. Anorg. Allg. Chem*. **2014**, *640*, 1789.

83. Papatriantafyllopoulou, C.; Raptopoulou, C. P.; Terzis, A.; Janssens, J. F.; Manessi-Zoupa, E.; Perlepes, S. P.; Plakatouras, J. C. *Polyhedron* **2007**, *26*, 4053.

84. Demir, S.; Kantar, G. K.; Topcu, Y.; Li, Q. *Transit. Met. Chem.* **2012**, *37*, 257.

85. Zhou, S.; Xue, X.; Wang, J.; Dong, Y.; Jiang, B.; Wei, D.; Wan, M. L.; Jia, Y. *J. Mater. Chem*. **2012**, *22*, 22774.

86. Allan, J. R.; Carson, B. R.; Gerrard, D. L.; Birnie, J. *Thermochim. Acta* **1990**, *160*, 329.

87. Liu, M. S.; Yu, Q. Y.; Cai, Y. P.; Su, C. Y.; Lin, X. M.; Zhou, X. X.; Cai, J. W. *Cryst. Growth Des.* **2008**, *8*, 4083.

88. Liptay, G.; Burger, K.; Mocsari-Fulop, E.; Porubszky, I. *J. Therm. Anal.* **1970**, *2*, 25.

89. Präbst, K.; Engelhardt, H.; Ringgeler, S.; Hübner, H. *Cell Viability Assays* **2017**, *1601*, 1

90. Mehta, A.; Patel, D.; Shah, K.; Shah, B.; Beladiya, J.; Chaudagar, K. *J. Pharm. Pharm. Sci*. **2017**, *6*, 2048.

91. Tang, J.; Yang, F.; Hou, M.; Huan, H.; Wang, H.; Li, K.; Fayyaz, S.; Shu, C.; Chang, H. *Semin. Cancer Biol.* **2019**, *58*, 109.

92. Wu, J.; Yi, W.; Jin, L.; Hu, D.; Song, B. *Cell div.* **2012**, *7*, 20.

93. Seeth, A.; Devaraj, H.; Sudhandiran, G. *J. Biochem. Mol. Toxicol*. **2020**, 34, 22433.

94. Xu, X.; Gao, X.; Jin, L.; Bhadury, P. S.; Yuan, K.; Hu, D.; Song, B.; Yang, S. *Cell division* **2011**, *6*, 1.

95. Cabrera, A. R.; Espinosa-Bustos, C.; Faúndez, M.; Meléndez, J.; Jaqued, P.; Daniliuce, C. G.; Aguirre, A.; Rojas, R. S.; Salasa, C. O. *J. Inorg. Biochem*. **2017**, *174*, 90.

96. Li, L.; Cao, W.; Zheng, W.; Fan, C.; Chen, T. *Dalton Trans*. **2012**, *41*, 12766.

97. Chen, T.; Liu, Y.; Zheng, W. J.; Liu, J.; Wong, Y. S. *Inorg. Chem*. **2010**, *49*, 6366.

98. Vilar, S.; Cozza, G.; Moro, S. *Curr. Top. Med. Chem.* **2008**, *8*, 1555.

99. Pearce, M. C.; Satterthwait, A. C.; Zhang, X.; Kolluri, S. K. *Apoptosis* **2019**, *24*, 1.

100. Thomsen, R.; Christensen, M. H. *J. Med. Chem.* **2006**, *49(11)*, 3315.

101. Vogler, M.; Walter, H. S.; Dyer, M. J. S. *Br. J. Haematol*. **2017**, *178*, 364.

102. Ramachandran, V.; Padmanaban, E.; Ponnusamy, K.; Naidub, S.; Natesan, M. *RSC Adv*. **2016**, *6*, 18946.

103. Abdolmaleki, A.; Ghasemi, B. J.; Ghasemi, F. *Chem. Biol. Drug. Des.* **2017**, *89*, 257.

104. Reid, T. E.; Fortunak, J. M.; Wutoh, A.; Wang, S. X. *Curr. Top. Med. Chem*. **2016**, *13*, 1452.